

# Enhancing GNSS Water Vapour Retrieval via Synergistic Microwave Radiometry: Thermodynamic Error Diagnosis and Bias Correction

Avinash N. Parde<sup>1</sup>, Christina Oikonomou<sup>1</sup>, Haris Haralambous<sup>1,2</sup>

<sup>1</sup>Frederick Research Center, Nicosia, 1303, Republic of Cyprus

<sup>2</sup>Frederick University, Nicosia, 1036, Republic of Cyprus

**Correspondence:** Avinash N. Parde ([aviparde07@gmail.com](mailto:aviparde07@gmail.com), [res.pav@frederick.ac.cy](mailto:res.pav@frederick.ac.cy))

## Abstract.

The retrieval of Precipitable Water Vapour (PWV) from Global Navigation Satellite Systems (GNSS) in thermodynamically complex environments is fundamentally limited by the accuracy of the weighted mean temperature ( $T_m$ ). This study evaluates the efficacy of static climatological models versus dynamic ground-based microwave radiometry for  $T_m$  determination in the Eastern Mediterranean, a region characterized by sharp refractivity gradients. Using the Cyprus GNSS Meteorology Enhancement [research project](#) (CYGMEN) infrastructure in Nicosia, the performance of the ERA5-based HGPT2 model and a co-located Microwave Radiometer (MWR) was assessed against radiosonde (RS) profiles during the 2025 warm season (Spring–Summer). Diagnostic analysis reveals that the static HGPT2 model fails to resolve the diurnal thermodynamic decoupling between the boundary layer and the free troposphere, leading to a systematic overestimation of  $T_m$  exceeding 6 K during peak solar insolation. Conversely, the MWR captures short-term thermodynamic variability ( $r=0.98$ ) but exhibits a systematic cold bias of  $-1.91$  K in raw retrievals. It is demonstrated that a site-specific linear bias correction reduces the MWR  $T_m$  Root Mean Square Error (RMSE) from 2.32 K to 1.43 K, significantly outperforming the empirical model. Sensitivity analysis confirms that thermodynamic uncertainty dominates the error budget, outweighing uncertainties in refractivity constants by an order of magnitude. Consequently, standard climatological retrievals diverge from the synergistic MWR-GNSS method during extreme hygrometric events, introducing systematic PWV biases exceeding 1.0 mm when moisture levels surpass 45 mm. The synergistic coupling of real-time radiometric  $T_m$  with GNSS data is therefore [essential-meaningful](#) for generating climate-quality PWV records in semi-arid coastal regions.

## 1 Introduction

Atmospheric water vapour (WV) is the primary greenhouse gas, contributing approximately 60% to the natural greenhouse effect and playing a vital role in regulating the Earth's thermodynamic budget (Kiehl and Trenberth, 1997; Trenberth et al., 2005). Furthermore, WV is the main driver of latent heat transport, influencing convective systems and global precipitation

30 patterns. High-frequency variations in Precipitable Water Vapor (PWV) correlate strongly with atmospheric instability and  
31 are a key factor in the initiation of severe weather. Specifically, rapid temporal gradients in PWV often precede heavy rainfall  
32 and flash floods, acting as a reliable precursor for convective storms (Brenot et al., 2013). Consequently, assimilating high-  
33 resolution PWV data into Numerical Weather Prediction (NWP) models significantly improves short-range precipitation  
34 "nowcasting" (Bennitt and Jupp, 2012). Accurate PWV retrieval is especially crucial for the Eastern Mediterranean (EM), a  
35 climate change "hotspot" warming faster than the global average (Giorgi, 2006; Lelieveld et al., 2012). This region is  
36 characterized by complex topography and land-sea contrasts, which create sharp atmospheric refractivity gradients. The  
37 Eastern Mediterranean EM faces a hydro-climatic paradox: a long-term drying trend ( $-0.5$  mm/decade) alongside increasing  
38 high-intensity, short-duration flash flood events (Zittis et al., 2019; Ziv et al., 2021). GNSS-derived PWV in this region exhibits  
39 strong diurnal cycles with amplitudes up to 5 mm, which are closely correlated with atmospheric instability (Ziskin Ziv et al.,  
40 2020). Despite this vulnerability, the Eastern Mediterranean EM currently lacks dense, continuous atmospheric profiling  
41 networks. Traditional observation methods, such as radiosondes (RS), fail to resolve these mesoscale events due to low  
42 temporal resolution (typically 12-hour intervals) and significant spatial gaps (Soden and Lanzante, 1996). While satellite-based  
43 passive remote sensing offers global coverage, it is often limited by revisit times, daylight dependence, or data degradation in  
44 coastal zones due to land contamination in the microwave footprint (Bennartz and Bauer, 2003).

45 These limitations underscore the necessity for ground-based remote sensing techniques that offer continuous, all-weather  
46 operability. Ground-based Global Navigation Satellite Systems (GNSS) meteorology has emerged as a robust technique for  
47 atmospheric sounding since the seminal proposal by Bevis et al. (1992). By estimating the Zenith Total Delay (ZTD) of GNSS  
48 signals traversing the neutral atmosphere, the Zenith Wet Delay (ZWD) can be isolated by subtracting the Zenith Hydrostatic  
49 Delay (ZHD), which is accurately modeled from surface pressure observations (Saastamoinen, 1972). GNSS-derived PWV  
50 offers significant advantages, including high temporal resolution (sub-hourly), all-weather availability, and cost-efficiency by  
51 leveraging existing geodetic infrastructure (Guerova et al., 2016; Jones et al., 2020).

52 The retrieval of PWV from GNSS ZWD relies on a dimensionless conversion factor,  $\Pi$ , which is a function of the  
53 atmospheric weighted mean temperature,  $T_m$ . Defined physically as  $\int (e/T) dz / \int (e/T^2) dz$  (Askne and Nordius, 1987),  $T_m$   
54 encapsulates the thermal state of the atmospheric column. The ~~accuracy of the derived PWV is linearly dependent on the~~  
55 ~~accuracy of  $T_m$ . Theoretical sensitivity analyses indicate that conversion factor ( $\Pi$ ) is nearly linearly proportional to  $T_m$ , a 1 K~~  
56 ~~error in  $T_m$  (assuming standard atmospheric temperatures near 280 K) introduces a relative error of approximately 0.36 % in~~  
57 ~~the final IWV. During severe moisture events with an IWV of  $50 \text{ kg m}^{-2}$ , this translates to an absolute error of  $\sim 0.18 \text{ kg m}^{-2}$ .~~  
58 ~~Consequently, a 1 % relative error in  $T_m$  translates strictly to a 1 % relative error in IWV. a 1 K error in  $T_m$  propagates to~~  
59 ~~approximately 0.3–0.5 mm bias in PWV, dominating the uncertainty budget ( $>50\%$ ) at high PWV levels ( $>50 \text{ mm}$ ) in empirical~~  
60 ~~models (Bevis et al., 1994; Jiang et al., 2019). Therefore, alongside the substantial errors inherent in ZTD estimation—such as~~  
61 ~~mapping function inaccuracies and surface pressure interpolation for the ZHD (Ning et al., 2016)—the determination of  $T_m$~~

62 ~~remains one of the primary sources of uncertainty in GNSS meteorology. Therefore, the determination of  $T_m$  is the primary~~  
63 ~~source of uncertainty in GNSS meteorology after ZTD estimation.~~ In the absence of in-situ profiles,  $T_m$  is commonly estimated  
64 using empirical regression models or global climatological models. However, earlier studies have demonstrated that empirical  
65  $T_m$  regressions, such as the Bevis model (Bevis et al., 1992), introduce relative PWV errors of 1–2% ~~(equivalent to 1–2 mm~~  
66 ~~RMSE)~~ due to weak  $T_s$ – $T_m$  correlations in coastal and equatorial regions, where annual/semiannual variations are not  
67 adequately captured (Yao et al., 2014; Lan et al., 2016). Similarly, global grid-based  $T_m$  models like GPT2w achieve RMSE  
68 <4 K at ~80% of mid-latitude sites but degrade in data-sparse areas like the Middle East and Africa, where reanalysis quality  
69 is limited (Böhm et al., 2015; Jiang et al., 2019). The Hourly Global Pressure and Temperature 2 (HGPT2) model represents  
70 a major advancement by providing hourly estimates derived from ERA5 reanalysis (Mateus et al., 2021). Despite recent  
71 validation of GPT2w and ECMWF models for Integrated Water Vapor (IWV) retrieval in the Mediterranean (Oikonomou et  
72 al. 2018), a critical gap exists: the quantification of vertical interpolation errors in these models, especially over complex  
73 coastal terrains. For instance, while recent validation studies in Cyprus demonstrate strong GNSS-PWV correlations (>0.6)  
74 with ERA5 during extreme precipitation, persistent reanalysis interpolation errors are highlighted in mountainous areas  
75 (Giannadaki et al., 2025). This lack of validation for HGPT2's performance in the complex topography of the Eastern  
76 Mediterranean EM potentially exacerbates PWV biases during extreme events.

77 An alternative approach to deriving  $T_m$  is the use of ground-based Microwave Radiometers (MWR). MWRs measure  
78 brightness temperatures at multiple frequencies to retrieve continuous vertical profiles of temperature and humidity. Ground-  
79 based MWRs have been shown to retrieve  $T_m$  with RMSE ~1–2 K in mid-latitudes, outperforming empirical models during  
80 synoptic anomalies (Cimini et al., 2010; Crewell and Löhnert, 2007; Löhnert et al., 2012). While multi-site intercomparisons  
81 reveal that MWR retrievals can exhibit upper-tropospheric cold biases (up to 5 K at >2 km altitude) (Van Malderen et al.,  
82 2014; Steinke et al., 2015), simple linear corrections can reduce RMSE by 20–40% (Ning and Elgered, 2021). Operational  
83 GNSS–MWR synergies for  $T_m$  bias correction have documented gains in PWV accuracy (10–30% RMSE reduction) in  
84 European networks (Vaquero-Martínez et al., 2018; Li et al., 2020). However, such applications are rare in the semi-arid EM,  
85 where MWR could critically mitigate reanalysis uncertainties.

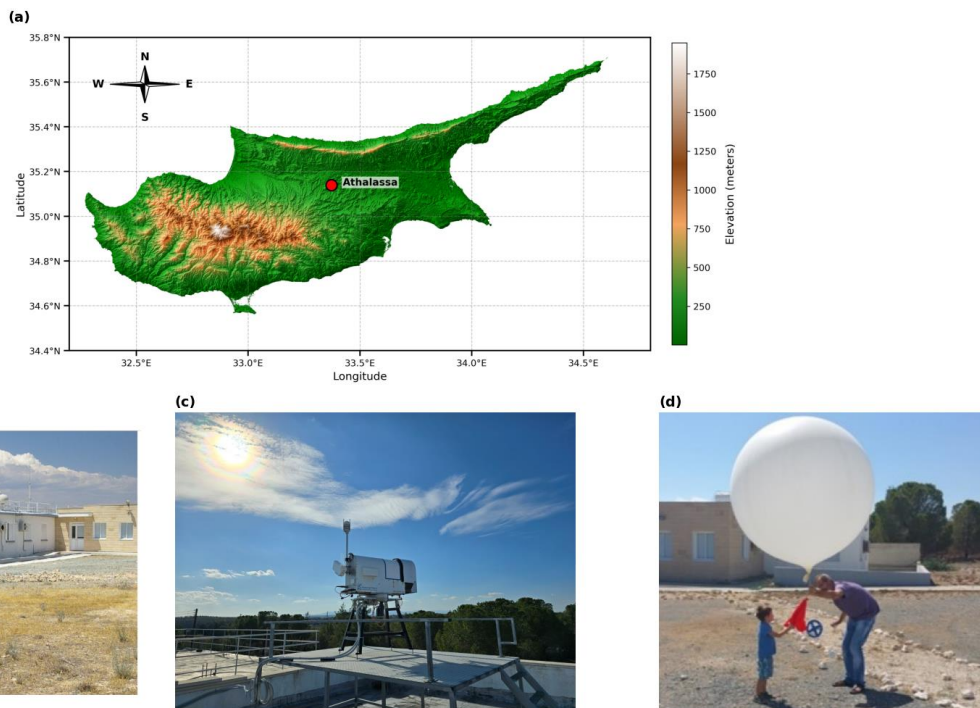
86 This study leverages the infrastructure of the CYGMEN (Cyprus GNSS Meteorology Enhancement) project, which is  
87 establishing a dense, multi-sensor meteorological network in Cyprus. The network, termed CyMETEO, integrates a dense  
88 array of continuous GNSS stations distributed across the island. Due to the high cost and operational complexity of radiometric  
89 profiling, the network currently features a single, centralized thermodynamic 'supersite' at the Athalassa observatory, where a  
90 GNSS receiver is strictly co-located with a MWR and a RS launch facility. The network, termed CyMETEO, integrates  
91 ~~continuous GNSS stations with co-located MWR and RS launch sites.~~ This unique instrumental setup provides an ideal testbed  
92 for inter-comparing atmospheric retrieval techniques in a coastal, semi-arid environment. The primary objective of this  
93 manuscript is to evaluate the accuracy of GNSS-derived PWV over the Eastern Mediterranean by assessing the performance  
94 of different  $T_m$  determination strategies. We specifically investigate the efficacy of the HGPT2 model compared to MWR-

95 derived  $T_m$  and RS benchmarks. The study aims to quantify the error budget of GNSS-PWV and determine whether the  
96 inclusion of MWR data provides statistically significant improvements over the state-of-the-art HGPT2 model. The manuscript  
97 is organized as follows: Section 2 describes the study area and the instrumentation of the ~~CYGMEN-CyMETEO~~ network;  
98 Section 3 details the methodology for GNSS processing, ZTD estimation, and the mathematical derivation of  $T_m$  from different  
99 sources; Section 4 presents the validation results and statistical analysis against RS reference data; and Section 5 concludes  
100 with recommendations for operational PWV monitoring strategies in the region.  
101

## 102 2 Data and Methodology

### 103 2.1 Observational Site and CYGMEN Infrastructure

104 The observational campaign was conducted at the Athalassa atmospheric observatory in Nicosia, Cyprus (35.15°N, 33.40°E,  
105 160 m a.s.l.), situated in the central Mesaoria plain. The site is characterized by complex topography, bounded by the Troodos  
106 Mountain to the southwest and the Pentadakylos Mountain to the north, as shown in Fig. 1a. This study presents the first  
107 comprehensive analysis of radiometric data acquired under the ~~Cyprus GNSS Meteorology Enhancement (CYGMEN)~~  
108 infrastructure project, established to monitor the thermodynamic state of the Eastern Mediterranean atmosphere. To ensure  
109 robust thermodynamic profiling and validation, three primary datasets were collated, as shown in Table 1:



110  
111 **Figure 1.** Location and instrumentation at Athalassa, Cyprus. (a) Site location on the island's elevation map. (b) GNSS reference station.  
112 (c) RPG-HATPRO radiometer. (d) Radiosonde balloon launching.

113 **Table 1:** Summary of Instrumentation and Datasets

Parameter	Microwave Radiometer (MWR)	Radiosonde (RS)	GNSS Station
<b>Instrument Model</b>	HATPRO-Gen5 (RPG)	Vaisala RS41-SGP	GNSS Receiver LEICA GR50 (Collocated)
<b>Role in Study</b>	Synergistic thermodynamic profiling (temperature and humidity) <u>and IWV estimation</u>	<i>In-situ</i> "Ground Truth" Reference	ZTD Source for PWV Retrieval
<b>Observation Type</b>	Passive remote sensing (22–58 GHz)	<i>In-situ</i> vertical profile (balloon-borne)	Continuous satellite signal delay
<b>Key Variables</b>	Brightness Temp ( $T_B$ ), $T(z)$ , $\rho_v(z)$ , IWV	$P(z)$ , $T(z)$ , $RH(z)$ , Geopotential Height	Zenith Total Delay (ZTD)
<b>Vertical Range</b>	Surface to 10 km (94 levels)	Surface to burst altitude (~30 km)	Column-integrated (single value)
<b>Temporal Resolution</b>	High frequency (~1 see raw, resampled to 15 min)	Periodic (launch dependent)	Continuous (high rate)
<b>Accuracy / Noise</b>	$T_B$ noise < 0.11 K (K-band), < 0.32 K (V-band)	$T$ : 0.3 K, $RH$ : 4_% (Manufacturer spec)	ZTD precision ~mm level
<b>Auxiliary Data</b>	Vaisala WXT536 (Rain, Surface Met)	GPS position/height	Surface Pressure

114

115 **2.2 Instrumentation and Data Processing**116 **2.2.1 Microwave Radiometry (MWR)**

117 The RPG-HATPRO radiometer observes downwelling atmospheric brightness temperatures ( $T_B$ ) across 14 channels: seven in  
118 the K-band (22–31 GHz) sensitive to water vapour, and seven in the V-band (51–58 GHz) sensitive to oxygen for temperature  
119 profiling. This instrument enables the continuous retrieval of temperature ( $T$ ) and absolute humidity ( $\rho_v$ ) profiles on a  
120 standardized grid of 94 vertical levels from the surface up to 10 km. The vertical resolution is optimized for the planetary  
121 boundary layer (PBL), ranging from 10–30 m up to 500 m, and decreasing to 100–500 m in the free troposphere. For this  
122 study, high-frequency MWR observations were resampled to 15-minute intervals to align with GNSS processing epochs. It is  
123 a well-documented limitation of passive microwave radiometry that retrieval accuracy degrades significantly during  
124 precipitation, as liquid water on the instrument's radome heavily contaminates the measured brightness temperatures. Because  
125 this study focused on the warm, dry season in the Eastern Mediterranean (March–October 2025), rainfall events were naturally  
126 sparse. Nevertheless, to ensure data integrity, real-time precipitation flags generated by the co-located Vaisala WXT536  
127 surface weather transmitter were utilized as a strict quality-control filter. Any MWR profiles retrieved during active

precipitation events were excluded from the dataset to prevent wet-radome anomalies from artificially skewing the thermodynamic bias analysis. To diagnose potential biases in the MWR-derived  $T_m$ , the dataset was split into a Training Set (April–June 2025) for regression modeling and a Validation Set (July–October 2025) for independent testing. In addition to thermodynamic profiling, the MWR's native retrieval algorithm possesses the capacity to directly estimate IWV from its K-band brightness temperatures.

### 2.2.2 Radiosonde Data Processing

To establish a rigorous validation dataset, Integrated Water Vapor (IWV) was derived from high-resolution vertical profiles obtained from collocated radiosonde launches. A strict collocation window was applied, where MWR profiles were averaged within  $\pm 30$  minutes of the balloon launch time. The raw telemetry data, comprising pressure ( $P$ ), temperature, and dew point temperature ( $T_d$ ), were processed to derive the total columnar water vapor content (in  $\text{kg m}^{-2}$ ) through the vertical integration of specific humidity, assuming the atmosphere is in hydrostatic equilibrium. The determination of the necessary moisture variables relied on the Magnus-Tetens approximation, which provides a widely accepted empirical relationship for saturation vapor pressure. First, the actual vapor pressure ( $e$ , in hPa) was computed directly from the dew point temperature ( $T_d$ , in  $^{\circ}\text{C}$ ). This calculation utilized the coefficients defined by Bolton (1980), which are optimized for saturation vapor pressure over liquid water in the meteorological temperature range, as shown in Eq. (1):

$$e = 6.112 \cdot \exp\left(\frac{17.67 \cdot T_d}{T_d + 243.5}\right) \quad (1)$$

Subsequently, the specific humidity ( $q$ , in  $\text{kg kg}^{-1}$ ) was derived via Eq. (2), representing the mass mixing ratio of water vapor to the total moist air parcel:

$$q = \frac{\epsilon \cdot e}{P - (1 - \epsilon) \cdot e} \quad (2)$$

where  $P$  is the static pressure (hPa) and  $\epsilon \approx 0.622$  represents the ratio of the molecular weight of water vapor to that of dry air. Once the specific humidity profile was established, the ~~total column~~ IWV was calculated by integrating  $q$  with respect to pressure. The retrieval algorithm employed the trapezoidal rule for numerical integration, which approximates the integral as the sum of discrete atmospheric layers (Eq. 3):

$$IWV = \frac{1}{g} \sum_{i=0}^{N-1} \frac{q_i + q_{i+1}}{2} \cdot |P_{i+1} - P_i| \quad (3)$$

where  $g$  is the gravity dependent on altitude,  $g(\phi, h)$ , where  $\phi$  represents the Geodetic latitude and  $h$  is the orthometric height.  $P$  is converted to Pascals ( $Pa$ ) prior to integration and  $N$  represents the total number of vertical levels in the RS profile. It should be noted that IWV, representing the mass column integral in  $\text{kg m}^{-2}$ , is physically and numerically equivalent to PWV expressed as a depth in millimeters (mm), assuming the standard density of liquid water ( $1000 \text{ kg m}^{-3}$ ). While the term IWV is frequently used when discussing direct profile integration from the MWR and RS, this study uses PWV (mm) as the standardized final retrieval metric to align with operational meteorological and forecasting conventions. It is important to note that while the nominal manufacturer uncertainty for the Vaisala RS41 humidity sensor is stated as 4 % for individual profile

160 measurements, the uncertainty of the resulting IWV is significantly lower. Because IWV is computed by integrating hundreds  
161 of discrete measurements across the vertical column (Eq. 3), uncorrelated random sensor noise is largely suppressed through  
162 statistical cancellation. Consequently, the integrated variables derived from the radiosonde, such as IWV and the  $T_m$ , possess  
163 the requisite precision to serve as a robust 'ground truth' standard for evaluating the finer relative uncertainties (1–2 %)   
164 associated with the GNSS and MWR retrievals. To ensure a rigorous, 'apples-to-apples' intercomparison with the active MWR,  
165 the radiosonde integration was strictly confined to a maximum altitude of 10 km Above Ground Level (AGL). This vertical  
166 cutoff was deliberately chosen to exactly match the 10 km ceiling of the standard RPG-HATPRO retrieval grid. While GNSS  
167 integrates delays through the entire atmosphere, bounding the in-situ reference data is mathematically necessary to isolate  
168 profiling performance. It is well established that this 10 km threshold does not introduce a systematic dry bias when comparing  
169 against total-column GNSS. Based on the mean radiosonde  $H_v$  of 1.51 km observed in this study, moisture decays exponentially  
170 (Eq. 812) such that the absolute humidity above 10 km is nearly zero. Furthermore, ambient temperatures at this altitude range  
171 from  $-40\text{ }^{\circ}\text{C}$  to  $-50\text{ }^{\circ}\text{C}$ , strictly limiting the saturation vapour pressure. Consequently, the residual water vapour between  
172 10 km and the tropopause is thermodynamically constrained to fractions of a millimeter, falling well below the nominal 4%  
173 measurement uncertainty of the Vaisala RS41 sensor itself.

### 175 2.2.3 GNSS Data Processing

176 ZTD estimates were derived from the collocated Leica GR50 receiver (station NICO) using the Tefnut PP software (Douša et  
177 al., 2014). The processing employed a Precise Point Positioning (PPP) strategy with an elevation cutoff angle of  $10^{\circ}$ . To  
178 account for tropospheric mapping errors, the Vienna Mapping Function 1 (VMF1) was applied. Station coordinates were  
179 constrained to the IGS14 reference frame, and satellite orbits and clock corrections were utilized from IGS Ultra-Rapid  
180 products. While IGS Final products are the gold standard for historical climate reprocessing due to their minimal orbital  
181 uncertainty, this study deliberately utilized IGS Ultra-Rapid products to evaluate the proposed synergistic retrieval architecture  
182 under near real-time operational constraints. Because a primary application of continuous GNSS-PWV is its assimilation into  
183 short-range NWP for severe weather 'nowcasting', it is crucial to assess system performance using the satellite orbits and clocks  
184 actually available during active forecasting. Although Ultra-Rapid products introduce a slight degradation in ZTD precision  
185 compared to Final products, this uncertainty (typically fractions of a millimeter in PWV) remains negligible compared to the  
186 massive, multi-millimeter systematic errors introduced by static thermodynamic modeling, which is the primary focus of this  
187 investigation. To isolate the ZWD, the ZHD was precisely calculated using continuous, co-located surface pressure  
188 observations obtained directly from the Vaisala WXT536 weather transmitter installed at the site, rather than relying on  
189 interpolated pressure fields ZTD values were estimated at 15-minute intervals, directly aligning with the temporal resolution  
190 of the MWR. It must also be noted that the computation of ZHD is fundamentally dependent on the assumed value of the dry  
191 refractivity constant,  $k_1$ . As established by Bevis et al. (1994) and further evaluated by Healy (2011), while  $k_1$  is known to a  
192 high degree of relative accuracy, its residual fractional uncertainty introduces a persistent systematic bias into the ZHD

193 estimation. Because ZWD is isolated by subtracting ZHD from the total delay, this  $k_I$ -induced bias directly propagates into the  
194 final IWV error budget, acting alongside the conversion uncertainties analyzed later in this study.  
195

## 196 2.3 Thermodynamic Modeling and Synergistic Retrieval Strategy

197 The conversion of GNSS-derived ZWD to PWV is governed by a proportionality factor,  $\Pi$ , whose accuracy is largely dictated  
198 by the  $T_m$ . To assess the fidelity of thermodynamic inputs for GNSS meteorology, we evaluated three distinct  $T_m$  derivation  
199 strategies. For profile-resolving instruments (MWR and RS),  $T_m$  values were computed by integrating the vertical profiles of  
200 physical temperature,  $T(z)$  (K), and absolute humidity,  $\rho_v(z)$  ( $\text{kg m}^{-3}$ ). Consistent with Bevis et al. (1992),  $T_m$  is defined as the  
201 mean temperature of the atmosphere weighted by the water vapour partial pressure, which can be expressed in terms of vapour  
202 density as shown in Eq. (4):

$$203 \quad T_m = \frac{\int_{z_{surf}}^{z_{top}} \rho_v(z) dz}{\int_{z_{surf}}^{z_{top}} \frac{\rho_v(z)}{T(z)} dz} \quad (4)$$

204 In practice, the continuous integrals were discretized using the trapezoidal rule from the surface ( $z_{surf}$ ) to the highest available  
205 profile level ( $z_{top}$ ). This approach assumes linear variation of  $T$  and  $\rho_v$  between measurement levels. For standalone GNSS  
206 retrieval (where no dynamic profiles are available),  $T_m$  was derived from the HGPT2 (Hourly Global Pressure and Temperature  
207 2) model (Mateus et al., 2021). HGPT2 is an advanced 'blind' empirical model, meaning its outputs are independent of the  
208 specific observational year. While dynamic NWP models provide superior real-time meteorological data, 'blind' models like  
209 HGPT2 remain heavily utilized in standard geodetic GNSS processing where real-time meteorological or NWP data streams  
210 are unavailable. It is constructed from a comprehensive 20-year historical baseline ~~HGPT2 is an advanced 'blind' empirical~~  
211 ~~model, meaning its outputs are independent of the specific observational year. It is constructed from a comprehensive 20-year~~  
212 ~~historical baseline~~ of atmospheric data from the ERA5 global reanalysis. Unlike standard static climatologies, HGPT2  
213 leverages the full ERA5 spatial resolution ( $0.25^\circ \times 0.25^\circ$ ) and provides temporal resolution at 1-hour intervals for any given Day  
214 of Year (DOY). It achieves this by employing a time-segmentation concept, modeling thermodynamic variables via long-term  
215 mean values combined with annual, semi-annual, and quarterly periodic functions.

216 To mitigate  $T_m$  errors in MWR, a supervised linear regression model was developed to calibrate the MWR observations. For  
217 robust independent validation, the collocated dataset was separated into two distinct temporal subsets: the ~~T~~training Set (April  
218 – June 2025), which was used to derive the regression coefficients, and the ~~v~~validation Set (July – October 2025), which was  
219 used exclusively to test the correction's performance on unseen data. A simple linear correction model was fitted to the training  
220 data using Ordinary Least Squares (OLS) minimization. The relationship is defined in Eq. (5) as:

$$221 \quad T_{m,corr} = \alpha \cdot T_{m,MWR} + \beta \quad (5)$$

222 where  $T_{m,corr}$  is the corrected MWR temperature,  $T_{m,MWR}$  is the raw  $T_m$  derived from the radiometer and  $\alpha$  (slope) and  $\beta$

(intercept) are the learned coefficients minimizing the residual sum of squares between the MWR and RS values. Based on our training Set (April–June 2025), the derived coefficients applied to the validation Set were  $\alpha = 1.0623$  and  $\beta = -15.6062$  K. To quantify the benefits of sensor synergy in integrated water vapour estimation, this study defines and contrasts two distinct GNSS PWV retrieval architectures. The first, “Standard Retrieval” which is a control method utilizes the  $ZTD_{GNSS}$  combined with the  $T_m$  derived empirically from the HGPT2 climatological model (Böhm et al., 2015). Second “Synergistic Retrieval” which proposed method couples  $ZTD_{GNSS}$  with a physical  $T_m$  derived directly from a collocated MWR. For the synergistic approach, the dimensionless conversion factor ( $\Pi$ ) was calculated dynamically using the MWR-derived  $T_m$  following Eq. (6) and Eq. (7).

$$PWV = \Pi \cdot ZWD \quad (6)$$

$$\Pi = \frac{10^6}{\rho_w R_v [k_2' + (k_3/T_m)]} \quad (7)$$

where  $\rho_w$  represents the density of liquid water ( $1000 \text{ kg m}^{-3}$ ) and  $R_v$  is the specific gas constant for water vapour ( $461.52 \text{ J kg}^{-1}\text{K}^{-1}$ ). To assess the sensitivity of the  $\Pi$  to the choice of thermodynamic coefficients, three widely used formulations were employed in this study, following Davis (1985)/Thayer (1974), Bevis et al. (1994), and Rüeger (2002), as shown in Table 2:

**Table 2.** Refractivity constants used in the sensitivity analysis of the  $\Pi$  factor, based on three commonly adopted formulations.

Method	$k_2$ (K hPa <sup>-1</sup> )	$k_3$ (K <sup>2</sup> hPa <sup>-1</sup> )	$k_2'$ (K hPa <sup>-1</sup> )
Davis (1985) / Thayer (1974)	64.79	$3.776 \times 10^5$	16.52
Bevis et al. (1994)	70.40	$3.739 \times 10^5$	22.13
Rüeger (2002)	71.295	$3.7546 \times 10^5$	22.97

To rigorously quantify the uncertainty in the final IWV (which is numerically equivalent to PWV) retrieval and avoid fragmented error attributions, standard error propagation must be applied to the fundamental conversion Eq. 6. Assuming the uncertainties in the wet delay and the conversion factor are uncorrelated, the variance of the final IWV ( $\sigma_{IWV}^2$ ) is expressed using partial derivatives as in Eq. 8:

$$\sigma_{IWV}^2 = \left(\frac{\partial IWV}{\partial ZWD}\right)^2 \sigma_{ZWD}^2 + \left(\frac{\partial IWV}{\partial \pi}\right)^2 \sigma_{\pi}^2 \quad (8)$$

Evaluating these primary partial derivatives yields the proportional contributions of the geodetic and thermodynamic components as shown in Eq. (9):

$$\sigma_{IWV}^2 = \pi^2 \sigma_{ZWD}^2 + ZWD^2 \sigma_{\pi}^2 \quad (9)$$

The uncertainty in the conversion factor ( $\sigma_{\pi}^2$ ) is itself a compound term driven by the  $T_m$  and the static atmospheric refractivity constants ( $k_2'$  and  $k_3$ ). Its variance is defined via partial derivatives as shown in Eq. (10):

$$\sigma_{\pi}^2 = \left(\frac{\partial\pi}{\partial T_m}\right)^2 \sigma_{T_m}^2 + \left(\frac{\partial\pi}{\partial k_2'}\right)^2 \sigma_{k_2'}^2 + \left(\frac{\partial\pi}{\partial k_3}\right)^2 \sigma_{k_3}^2 \quad (10)$$

The sensitivity of the conversion factor strictly to  $T_m$  (the dynamic thermodynamic variable evaluated in this study) is quantified by its partial derivative and it represented as Eq. (11):

$$\frac{\partial\pi}{\partial T_m} = \pi \left[ \frac{k_3}{T_m^2 (k_2' + \frac{k_3}{T_m})} \right] \quad (11)$$

This consolidated formulation establishes the exact mathematical limits of thermodynamic error propagation. As demonstrated in the sensitivity analysis (Section 3.4), this framework accurately isolates the dynamic uncertainties driven by  $T_m$  from the baseline static biases introduced by the chosen refractivity constants.

## 2.4 Diagnostic Parameters and Error Analysis

The vertical structure of the atmosphere was analyzed by segregating the dataset into two regimes: the PBL (0–2 km), where water vapor is concentrated, and the Free Troposphere (> 2 km). Additionally, the scale height ( $H_v$ ) was calculated to quantify the vertical distribution of moisture. This parameter is crucial because it provides a single, representative value for the rate at which water vapor decreases with altitude, which is a key factor in understanding atmospheric stability, cloud formation, and radiative transfer processes.  $H_v$  was derived for both RS and MWR by fitting an exponential decay function (Eq. 812) to the absolute humidity profile ( $\rho_v$ ). This curve fitting was deliberately restricted to the lowest 4 km of the atmosphere because this layer contains the vast majority (>90%) of the tropospheric water vapor mass. As established in climatological studies (e.g., Trenberth et al., 2005; Weaver and Ramanathan, 1995), atmospheric water vapor decays exponentially with a typical scale height of 1.5 to 2.5 km. Above 4 km, moisture levels approach the noise floor of both the MWR and the RS sensors, and the profile frequently deviates from a standard exponential decay due to complex layering or subsidence inversions. Forcing an exponential fit over the entire 10 km column causes the algorithm to heavily weight near-zero, noisy upper-tropospheric values, which mathematically degrades the curve fit for the boundary layer where the bulk mass actually resides (Tomasi, 1984). Therefore, the 4 km limit is a necessary mathematical boundary to ensure a physically meaningful fit.

$$\rho_v(z) = \rho_{v,0} \cdot \exp\left(-\frac{z}{H_v}\right) \quad (812)$$

where  $\rho_v(z)$  is the absolute humidity at height  $z$ , and  $\rho_{v,0}$  is the surface humidity. Furthermore, the scale height metric fundamentally assumes the atmosphere conforms to a well-behaved exponential decay. During complex meteorological states—such as deep convective mixing, strong elevated moist layers, or severe shallow inversions—the true vertical moisture distribution breaks this exponential assumption. Forcing a mathematical fit onto these non-exponential profiles yields physically meaningless artifacts. Therefore, a Quality Assurance filter was applied, bounding the analysis to the physically realistic range of  $0.1 \text{ km} < H_v < 4.0 \text{ km}$ . Profiles yielding values outside this range were discarded because they indicate the

280 underlying exponential model itself is invalid for that specific atmospheric profile, preventing artificial statistical skewing in  
 281 the instrument intercomparison. Profiles yielding  $H_v$  values outside the physically realistic range of 0.1 to 4.0 km were excluded  
 282 from the statistical analysis. To evaluate the performance limitations of standard climatological models under varying  
 283 hygrometric conditions, the systematic error ( $\Delta PWV$ ) was defined as the residual between the synergistic and standard  
 284 approaches (Eq. 913):

$$\Delta PWV = PWV_{Synergistic} - PWV_{Standard} \quad (913)$$

285  
 286 The dataset was stratified into discrete bins of 5 mm PWV to isolate regimes of moisture abundance~~thermodynamic severity~~.  
 287 Within each bin, the mean bias and  $\pm 1\sigma$  uncertainty were computed. These statistics were utilized to determine the "~~Critical~~  
 288 ~~Error Culmination~~Systematic Bias Threshold," defined herein as the specific hygrometric threshold where the systematic  
 289 model error exceeds 1 mm. Finally, the propagation of thermodynamic uncertainty into the moisture retrieval was quantified  
 290 via linear regression analysis. This compared the relative error in  $T_m$  (HGPT2 vs. MWR) against the resulting relative error in  
 291 PWV, serving as an empirical verification of the theoretical sensitivity approximation given in Eq. (104):

$$\frac{\Delta PWV}{PWV} \approx \frac{\Delta T_m}{T_m} \quad (104)$$

### 293 3 Results 294

295 The following evaluation follows a top-down diagnostic approach. First, the macroscopic baseline performance of the final  
 296 derived moisture products is established. Subsequently, the underlying thermodynamic variables driving these discrepancies  
 297 are isolated, culminating in the development of a targeted calibration scheme to mitigate the identified biases.

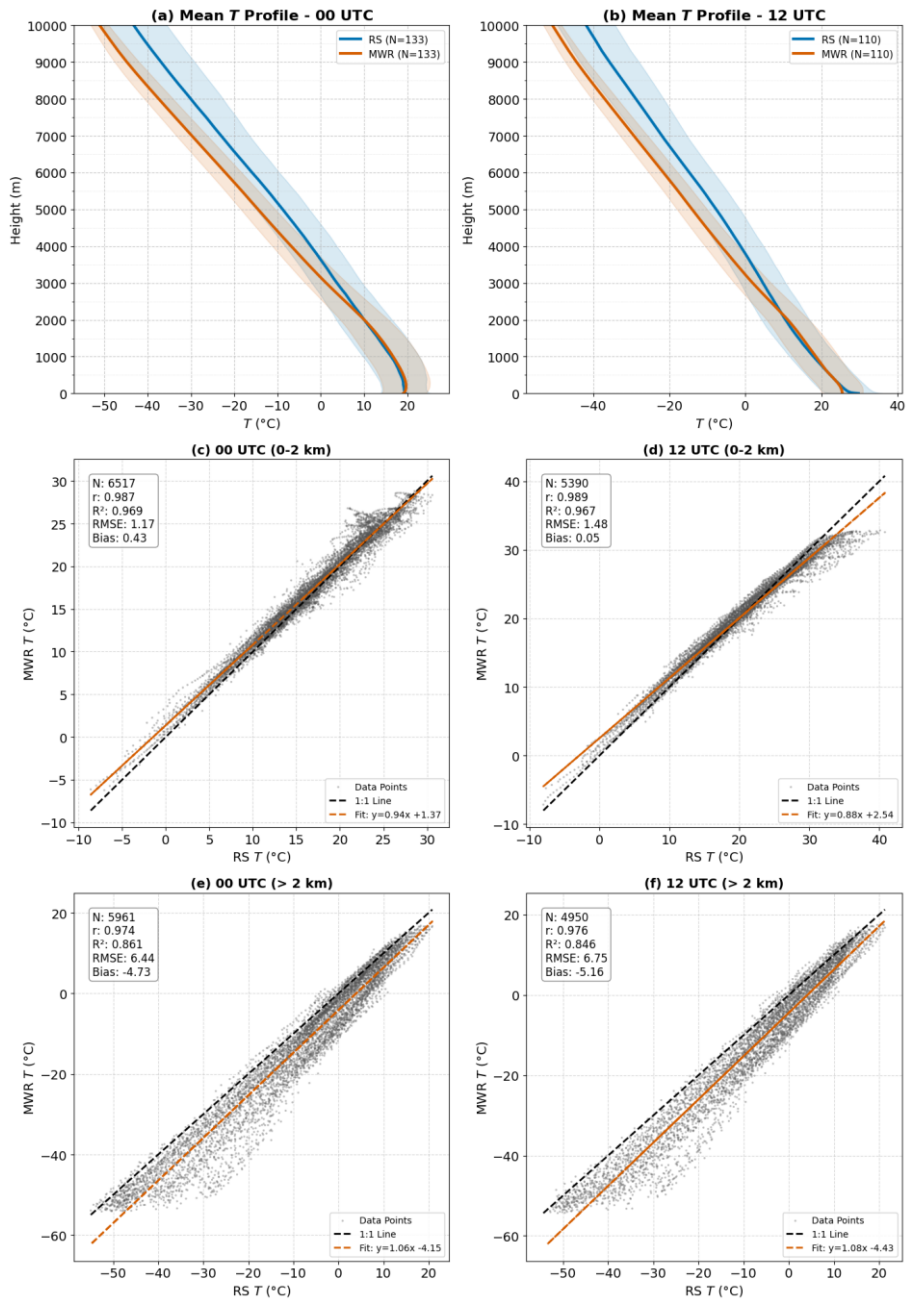
#### 298 3.1 Temperature and Humidity Profile Validation

299 MWR-retrieved temperature  $T$  and  $\rho_v$  profiles were validated against collocated RS observations at 00:00 UTC and 12:00 UTC  
 300 during March–October 2025. Profiles were stratified into the planetary boundary layer (PBL; 0–2 km) and free troposphere  
 301 (>2 km), as shown in Figs. 2 and 3. Mean vertical temperature profiles show agreement between MWR and RS (Fig. 2a–b).  
 302 In the boundary layer (0–2 km), MWR retrieves temperature with high precision ( $r > 0.98$ ,  $RMSE < 1.5$  K). Above 2 km, a cold  
 303 bias is observed in the MWR retrieval, reaching  $-5.16$  K at 12 UTC (Fig. 2f). Despite this bias, the linearity remains strong  
 304 ( $r \approx 0.97$ ), indicating the sensor captures relative thermal variations aloft despite the absolute offset. This confirms the trend  
 305 observed in the mean profiles, where the MWR underestimates temperatures in the mid-to-upper troposphere. Consequently,  
 306 the RMSE increases substantially to approximately  $6.4$ – $6.7$   $^{\circ}\text{C}$ . The stark contrast in accuracy between the lower and upper  
 307 troposphere is a known characteristic of ground-based microwave radiometry (Parde et al., 2025; Pakkattil et al., 2025). The  
 308 high accuracy below 2 km is attributed to the high information content of the opaque V-band channels (51–58 GHz), whose  
 309 weighting functions peak near the surface. Above 2 km, these weighting functions broaden significantly, reducing vertical

310 resolution and causing a "smearing" effect where the instrument provides a volume-averaged temperature rather than a precise  
311 point measurement. The observed cold bias is likely a result of the retrieval algorithm (e.g., neural network) relying heavily  
312 on a climatological *a priori* dataset that does not perfectly represent the thermal conditions of the transition season observed,  
313 or systematic offsets in the radiative transfer model (absorption coefficients) used for training.

314 The mean  $\rho_v$  profiles (Figs. 3a–b) show the expected exponential decrease of moisture with height. At 00 UTC, the profiles  
315 align reasonably well. However, at 12 UTC, the MWR profile exhibits a structural deviation between 1–2 km, failing to capture  
316 the smooth moisture gradient recorded by the RS. This discrepancy may be attributed to the MWR's limited vertical resolution  
317 during periods of active daytime mixing or complex humidity layering. The retrieval of humidity in the lower atmosphere  
318 shows moderate agreement but is less accurate than the temperature retrievals. Performance is notably better at night (00 UTC)  
319 with  $r$  of 0.878 and RMSE of  $1.98 \text{ g m}^{-3}$ . At 12 UTC, the correlation drops to 0.744, and the scatter increases (RMSE =  $2.31 \text{ g}$   
320  $\text{m}^{-3}$ ). A negative bias persists at both times ( $-0.51 \text{ g m}^{-3}$  at 00 UTC and  $-0.91 \text{ g m}^{-3}$  at 12 UTC), indicating a tendency for the  
321 MWR to underestimate moisture content in the boundary layer, particularly during the day. Surprisingly, the statistical linearity  
322 for  $\rho_v$  improves slightly or remains stable above 2 km, likely due to the lower overall magnitude of humidity at these heights.  
323 The correlation coefficients remain stable ( $\sim 0.87$ ). In contrast to the lower levels, the bias shifts to slightly positive values  
324 ( $0.23 \text{ g m}^{-3}$  at 00 UTC and  $0.46 \text{ g m}^{-3}$  at 12 UTC), suggesting a slight moist bias in the MWR retrievals aloft. The linear fits  
325 (Figs. 3e–f) align closely with the 1:1 line, with slopes near unity (0.90 and 1.00), indicating that the MWR effectively captures  
326 the free tropospheric humidity trends despite the lower absolute values. The difficulty in retrieving accurate  $\rho_v$  profiles,  
327 particularly at 12 UTC, stems from the limited vertical resolution of the K-band channels (22–31 GHz). Unlike temperature  
328 profiling, humidity profiling offers very few independent degrees of freedom (typically  $<3$ ), making it difficult for the MWR  
329 to resolve sharp vertical gradients often present at the top of the convective boundary layer during the daytime. The structural  
330 deviation and underestimation are common issues linked to the "smoothing" error inherent in passive radiometry, where sharp  
331 moisture inversions are averaged out. Furthermore, the persistent bias suggests potential uncertainties in the water vapor  
332 absorption models (spectroscopic parameters) or non-representative training data used in the retrieval algorithm.

333



334

335 Figure 2. Comparison of radiosonde and microwave radiometer (MWR) temperature profiles: (a–b) Mean vertical temperature  
 336 (T) profiles at 00 and 12 UTC with variability shading; (c–f) Scatter comparisons for the lower (0–2 km) and upper (>2 km)  
 337 atmosphere at both times.

338

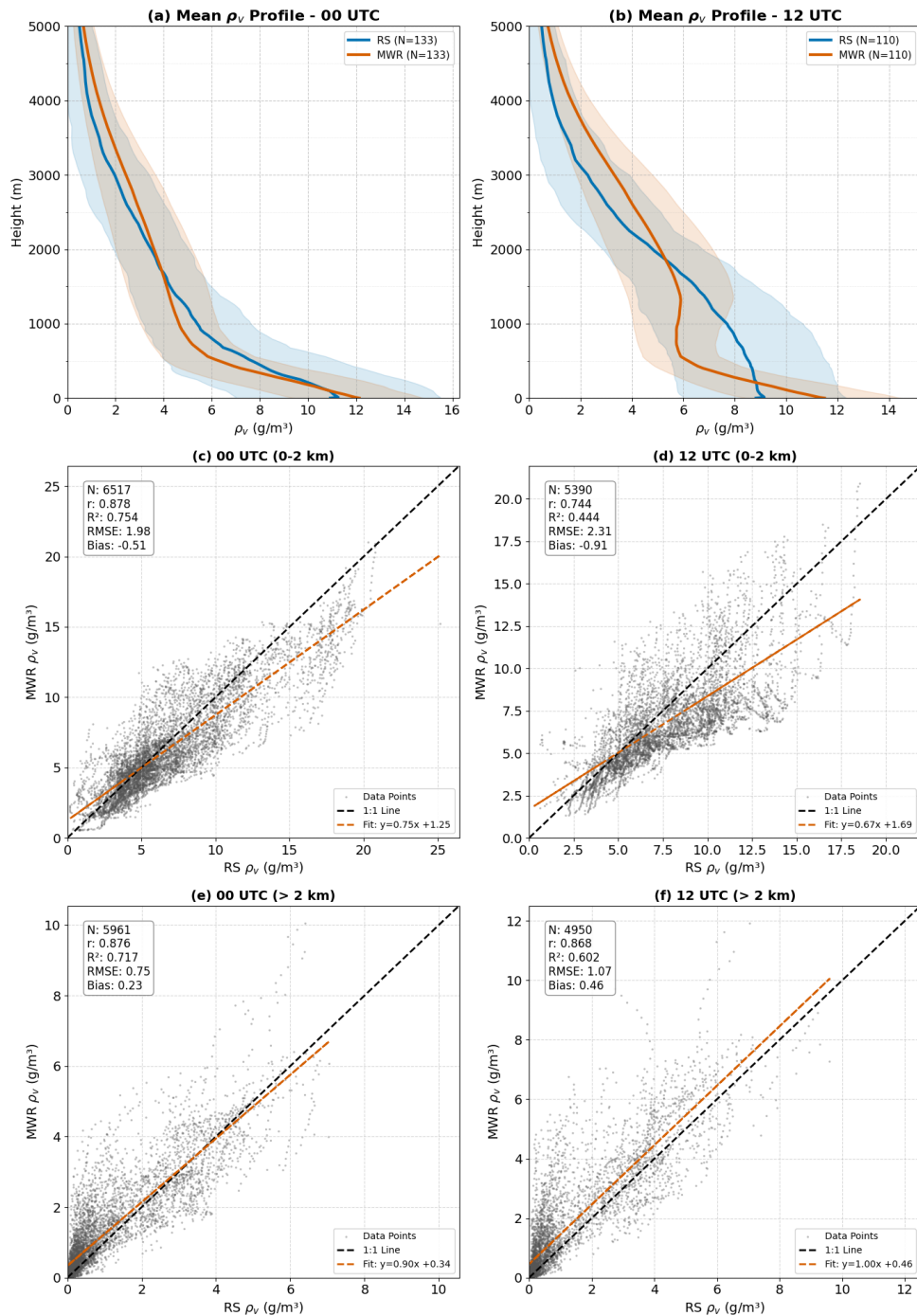
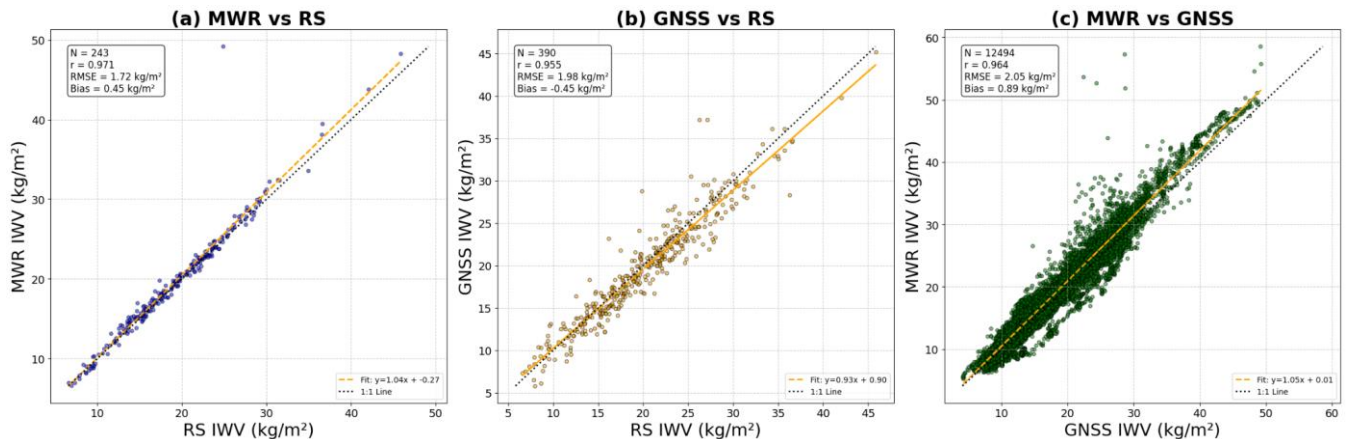


**Figure 3.** Comparison of radiosonde and microwave radiometer (MWR) absolute humidity ( $\rho_v$ ) profiles: (a–b) Mean vertical  $\rho_v$  profiles at 00 and 12 UTC with variability shading; (c–f) Scatter comparisons for the lower (0–2 km) and upper (>2 km) atmosphere at both times.

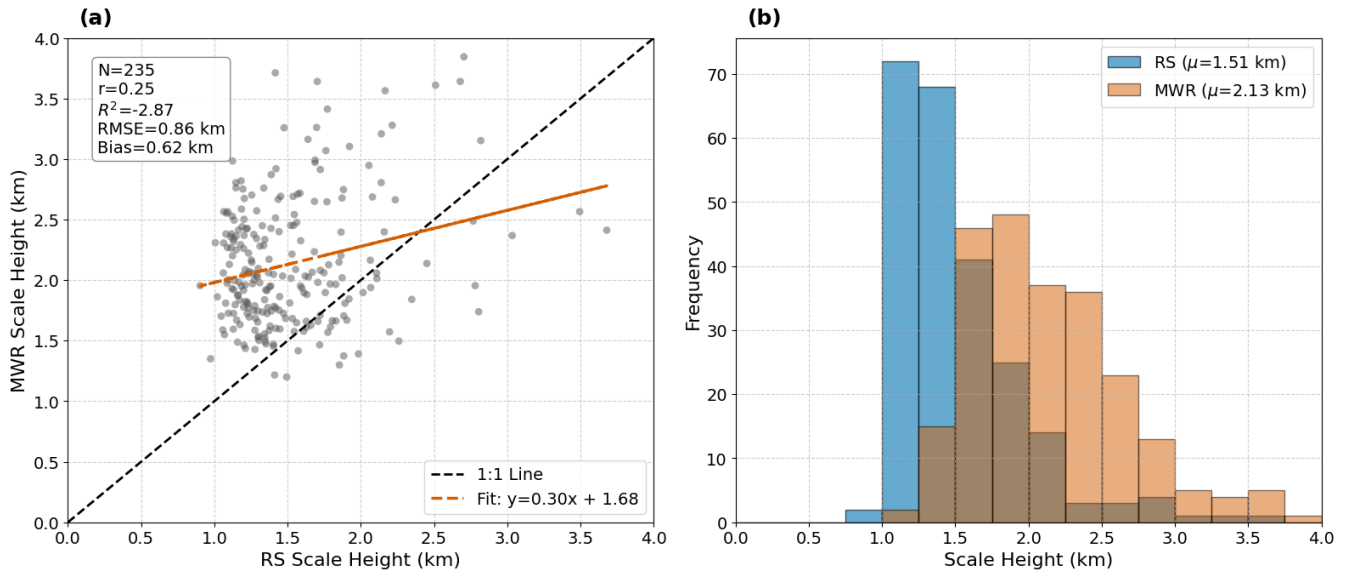
### 3.2 Integrated Water Vapour (IWV) and Scale Height ( $H_v$ ) Validation

344 Unlike vertical profiling, the MWR excels in measuring total column quantities. The comparison with RS yields an excellent  
 345 correlation ( $r=0.971$ ) and a low RMSE of  $1.72 \text{ kg m}^{-2}$ . This performance disparity—superior IWV versus degraded profiles—  
 346 confirms that while the sensor cannot resolve vertical structural details due to smoothing error, the radiometric brightness  
 347 temperature in the K-band remains strictly proportional to the total precipitable water mass. The GNSS-derived IWV shows a  
 348 slight negative bias relative to RS ( $-0.45 \text{ kg m}^{-2}$ ), whereas it relative to the MWR exhibits a positive bias ( $+0.45 \text{ kg m}^{-2}$ ). The  
 349 cumulative offset observed in the MWR-GNSS intercomparison ( $+0.89 \text{ kg m}^{-2}$ ) highlights the systematic differences in  
 350 calibration and retrieval assumptions between active (GNSS) and passive (MWR) techniques. The GNSS underestimation is  
 351 likely driven by errors in the  $T_m$  derived from the static HGPT2 model, a hypothesis further explored in Section 3.4. The  
 352 derivation of the  $H_v$  is admittedly a crude, single-parameter representation of the complex atmospheric moisture profile.  
 353 However, it is utilized in this study specifically as a diagnostic metric to quantify the structural limitations of passive  
 354 microwave remote sensing. The comparison of  $H_v$  calculated from RS and MWR profiles is shown in Fig. 5. Unlike the high-  
 355 fidelity IWV retrievals, the MWR-derived scale height shows negligible correlation with RS observations ( $r=0.25$ ,  $R^2=-2.87$ )  
 356 and a massive systematic positive bias of 0.62 km. The histograms (Fig. 5b) further elucidate this discrepancy: while the RS  
 357 scale heights follow a narrow, physically realistic distribution centered around a mean ( $\mu$ ) of 1.51 km, the MWR distribution  
 358 is artificially broad and shifted to significantly higher values ( $\mu=2.13 \text{ km}$ ). The limitation of passive microwave profiling is  
 359 most evident in the derivation of the water vapor  $H_v$ . The MWR-derived  $H_v$  shows negligible correlation with RS ( $r=0.25$ ) and  
 360 a systematic positive bias of 0.62 km. As detailed in Figure 5, the MWR distribution is artificially shifted toward higher values.  
 361 This "stretching" effect is a direct artifact of the smoothing error; by failing to resolve the rapid moisture decrease at the PBL  
 362 top, the retrieval algorithm smears the moisture profile upward, mathematically inflating the calculated e folding depth.  
 363 Therefore, while MWR is a primary standard for IWV, it should not be relied upon for characterizing vertical moisture  
 364 compactness without synergistic constraints.



365 **Figure 4.** Intercomparison of integrated water vapour (IWV) retrieved from Microwave Radiometer (MWR), GNSS, and Radiosonde  
 366 observations. (a) MWR IWV versus radiosonde IWV, (b) GNSS IWV (derived using HGPT2  $T_m$ ) versus radiosonde IWV, and (c) MWR  
 367 IWV versus GNSS IWV (derived using HGPT2  $T_m$ ).  
 368

369 The large scatter and ambiguity in the MWR estimates—which completely dwarf the individual least-squares fit  
370 uncertainties of the exponential regression—are a direct consequence of the instrument's physical limitations.  $H_v$  is highly  
371 sensitive to the sharp vertical gradient of humidity at the top of the planetary boundary layer. However, the K-band channels  
372 (22–31 GHz) utilized for humidity profiling possess broad weighting functions, restricting the vertical degrees of freedom to  
373 typically fewer than three. Because the MWR lacks the vertical resolution to capture sharp moisture inversions, the retrieval  
374 algorithm mathematically smears the moisture mass upward. This inherent 'smoothing error' artificially elongates the vertical  
375 moisture profile, effectively inflating the calculated e-folding depth. Therefore, the inclusion of this  $H_v$  analysis serves to  
376 transparently demonstrate a critical operational boundary: while the MWR is an excellent standard for IWV, it is fundamentally  
377 unreliable and mathematically unsuited for characterizing vertical moisture compactness. The significant deviations observed  
378 in these macroscopic retrieval products necessitate a deeper investigation into the intermediate thermodynamic variables  
379 driving the conversion process. Consequently, the isolated performance of the  $T_m$  is evaluated in Section 3.3, followed by the  
380 introduction of a post-retrieval MWR calibration scheme in Section 3.4 designed to mitigate these native biases. The water  
381 vapor  $H_v$ , which describes the exponential decay of moisture with altitude, was calculated for both RS and MWR profiles. The  
382 comparison is shown in Fig. 5. Unlike the IWV, the derived scale height from MWR shows poor agreement with RS  
383 observations (Fig. 5a). The correlation is weak ( $r=0.25$ ), and the coefficient of determination is negative ( $R^2=-2.87$ ), indicating  
384 that the MWR derived scale height has no predictive power for the true atmospheric scale height. The MWR consistently  
385 overestimates  $H_v$ , with a significant positive bias of 0.62 km and a regression slope (0.30) that is far flatter than the 1:1 line.  
386 The histograms (Fig. 5b) further elucidate this discrepancy. The RS scale heights (blue bars) follow a narrow distribution  
387 centered around a mean ( $\mu$ ) of 1.51 km, typical for the study region. In contrast, the MWR distribution (orange bars) is much  
388 broader and shifted significantly to higher values ( $\mu=2.13$  km). The MWR rarely computes scale heights below 1.5 km, whereas  
389 the RS frequently observes compact moisture layers with scale heights near 1.0–1.2 km. The failure of the MWR to accurately  
390 derive scale height is a direct consequence of the physical limitations of passive microwave remote sensing.  $H_v$  is highly  
391 sensitive to the sharp vertical gradient of humidity ( $\partial z/\partial p_v$ ) at the top of the boundary layer. The K-band channels (22–31 GHz)  
392 utilized for humidity profiling possess broad weighting functions, which limits the vertical degrees of freedom to typically  
393 fewer than three. Because the MWR lacks the vertical resolution to capture sharp moisture inversions, the retrieval algorithm  
394 mathematically smears the moisture mass upward. This inherent smoothing effect artificially elongates the vertical moisture  
395 profile, effectively increasing the calculated e-folding depth. This confirms that while the MWR is a robust standard for total  
396 column water (IWV), a single parameter exponential fit like  $H_v$  is inadequate for characterizing vertical moisture compactness  
397 using passive radiometry. This result highlights a critical limitation: while MWR is excellent for total column water (IWV), it  
398 is not reliable for characterizing the vertical compactness of the moisture layer ( $H_v$ ).

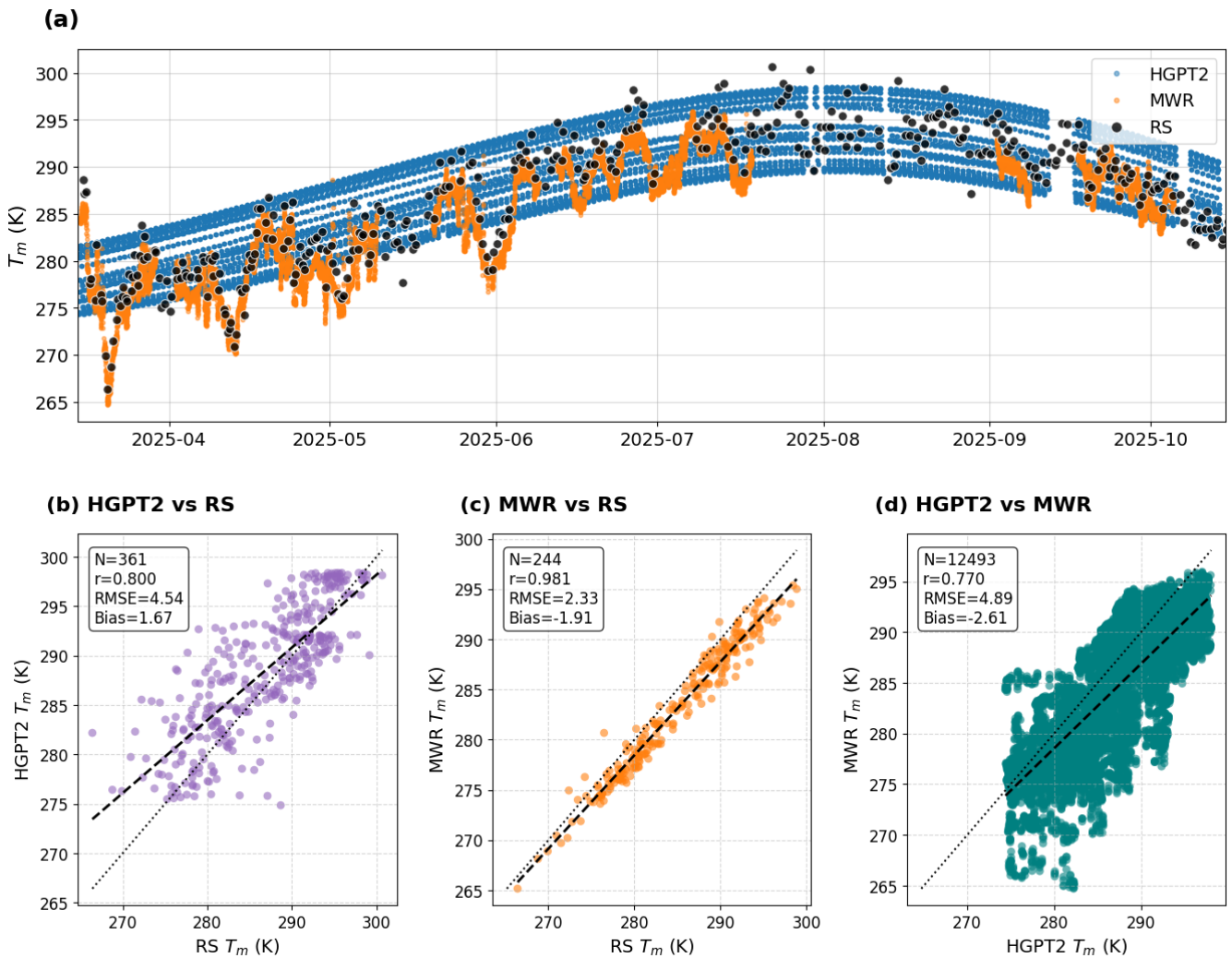


399  
400 **Figure 5:** Comparison of scale height from radiosonde (RS) and microwave radiometer (MWR): (a) Scatter plot with 1:1 line and linear fit,  
401 including summary statistics; (b) Frequency distributions showing mean scale heights for RS and MWR.  
402

### 403 3.3 Weighted Mean Temperature ( $T_m$ ) Validation

404 The accurate estimation of the  $T_m$  is critical for converting GNSS-derived ZWD into PWV. The performance of  $T_m$  derived  
405 from the MWR and the empirical GPT2w model (HGPT2) was evaluated against RS measurements, which serve as the "ground  
406 truth." The results are presented in Fig. 6. The time series (Fig. 6a) illustrates the seasonal evolution of  $T_m$  from April to October  
407 2025. The Radiosonde observations (black dots) show significant variability, capturing synoptic-scale weather fluctuations.  
408 The MWR-derived  $T_m$  (orange dots) tracks these fluctuations with remarkable precision, overlaying the RS points almost  
409 perfectly. In stark contrast, the HGPT2 model (blue dots) provides a smooth, climatological curve. While it captures the general  
410 seasonal trend, it completely misses the day-to-day thermodynamic variability, often overestimating  $T_m$  during cooler transient  
411 events and underestimating it during warmer anomalies. The empirical model shows only moderate performance ( $r=0.800$ )  
412 with a substantial spread ( $RMSE = 4.54$  K). A systematic positive bias of 1.67 K indicates that HGPT2 generally overestimates  
413 the atmospheric temperature profile in this region. The scatter plot reveals a diffuse, "cloud-like" distribution, confirming its  
414 inability to capture real-time atmospheric dynamics. The MWR demonstrates superior performance, achieving a near-perfect  
415 correlation ( $r=0.981$ ). The RMSE is significantly reduced to 2.33 K, which is nearly half the error of the empirical model.  
416 Interestingly, the MWR exhibits a negative bias of  $-1.91$  K, suggesting a systematic underestimation of  $T_m$ . Crucially, this bias  
417 does not originate in the free troposphere, but rather in the planetary boundary layer (0–3 km). Since  $T_m$  is weighted by water  
418 vapour pressure, this "cold bias" indicates the MWR is underestimating the intense near-surface heating or the sharp lapse  
419 rates characteristic of the Nicosia environment. Despite this offset, the tight linearity indicates that MWR is an excellent source  
420 for capturing real-time  $T_m$  variations. Comparing the large dataset of MWR against HGPT2 ( $N=12,493$ ) confirms the

421 discrepancy between dynamic and static modeling. The correlation is lower ( $r=0.770$ ) and the scatter is large (RMSE = 4.89  
 422 K), further proving that static empirical models are insufficient for high-precision GNSS meteorology compared to dynamic  
 423 radiometer measurements. While errors in ZTD estimation contribute significantly to the overall uncertainty budget, the  
 424 specific error introduced during the conversion from delay to water vapour is linearly dependent on the accuracy of  $T_m$ .  
 425 Assuming a given ZTD, a standard rule of thumb states that a 1 % relative error in  $T_m$  translates to roughly a 1 % relative error  
 426 in the resulting PWV. The accuracy of PWV retrieval from GNSS is linearly dependent on the error in  $T_m$ . A standard rule of  
 427 thumb states that a 1% error in  $T_m$  translates to roughly a 1% error in PWV. By switching from a static model (HGPT2, ~4.5  
 428 K error) to a dynamic sensor (MWR, ~2.3 K error), the uncertainty in the GNSS water vapour product is effectively halved.  
 429 This validates the "synergistic" approach of using collocated MWR thermal data to process GNSS signals.



430

431 **Figure 6.** Comparison of weighted mean temperature ( $T_m$ ) derived from HGPT2, MWR, and Radiosonde (RS) during March–November  
432 2025. (a) Time series of  $T_m$  estimates from all three sources. (b–d) Scatter plots showing statistical comparisons between: (b) HGPT2 vs.  
433 RS, (c) MWR vs. RS, and (d) HGPT2 vs. MWR.

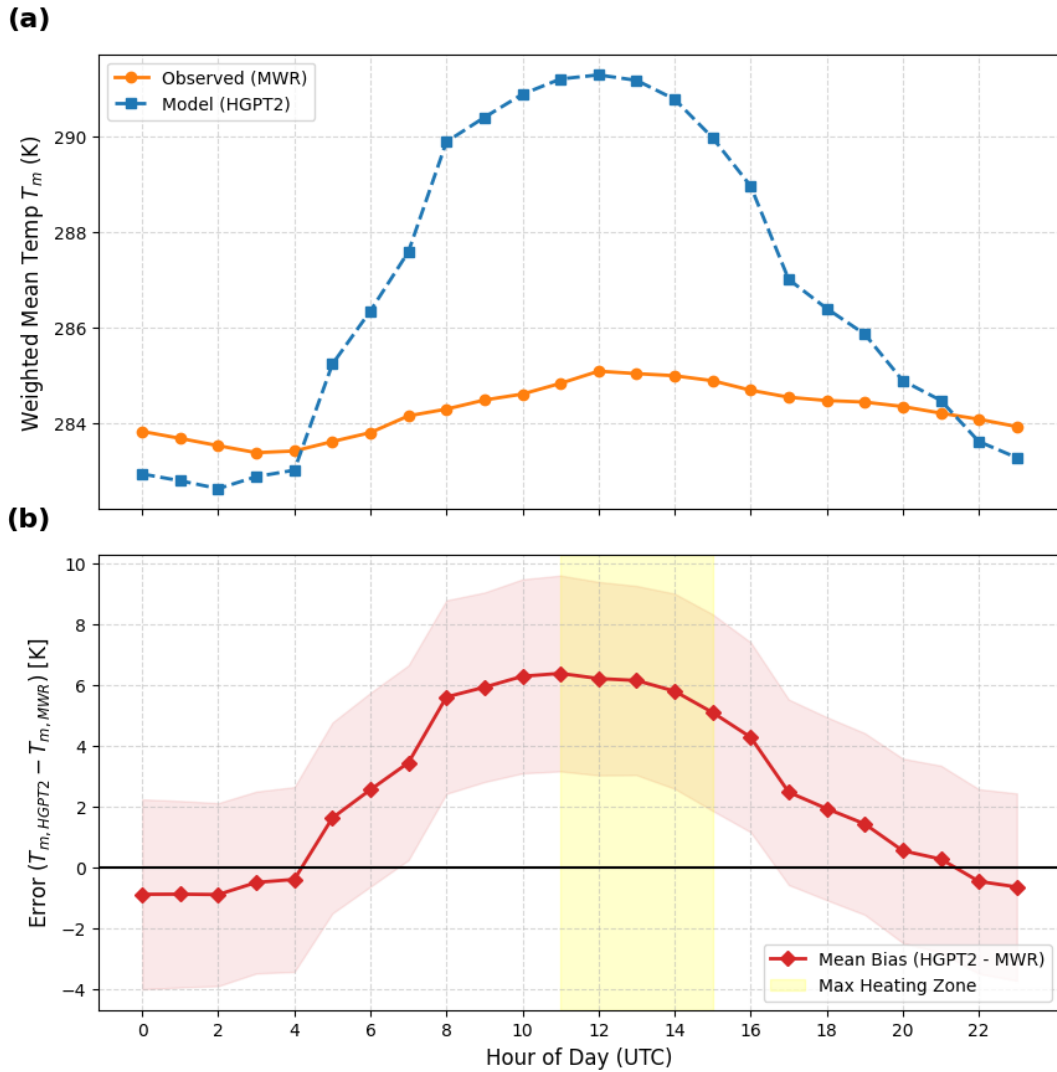
434

### 435 **3.4 Diagnostic Analysis of ~~Thermodynamic Errors~~ Thermodynamic Conversion Uncertainty**

#### 436 **3.4.1 Diurnal Bias Amplification in Static Models**

437 To pinpoint the physical origin of the HGPT2 model's deficiency, a diurnal cycle analysis was performed (Fig. 7). While the  
438 previous statistical metrics indicated a general positive bias, the temporal breakdown in Fig. 7a reveals that this error is not  
439 uniform, but is driven by a fundamental misrepresentation of atmospheric thermodynamics. The MWR-derived  $T_m$  (orange  
440 line) exhibits a physically realistic, dampened diurnal amplitude of approximately 1.5 K. This stability reflects the high thermal  
441 inertia of the tropospheric column, which does not heat rapidly in response to surface insolation. In stark contrast, the HGPT2  
442 model (blue line) displays an exaggerated diurnal wave with an amplitude exceeding 8.5 K, peaking synchronously with solar  
443 noon (12:00 UTC). ~~As previously documented in the literature (Wang, 2005; Bock, 2021), deriving  $T_m$  via empirical regression  
444 on surface skin temperature ( $T_s$ ) is known to introduce spurious diurnal cycles. Our observations confirm this intrinsic  
445 limitation: because the empirical model's periodic functions are overly sensitive to  $T_s$ , it assumes intense skin-level heating  
446 propagates uniformly through the column, failing to capture the true thermodynamic decoupling between the turbulent  
447 planetary boundary layer and the stable free troposphere. This exaggerated daytime amplitude suggests that the empirical  
448 model's periodic functions are overly sensitive to surface skin temperature ( $T_s$ ). More importantly, because  $T_m$  is fundamentally  
449 defined as a moisture-weighted integral, the diurnal evolution of specific humidity plays a critical, coupled role in this error.~~  
450 During the hours of peak solar insolation (11:00–14:00 UTC), the coastal environment experiences active convective mixing  
451 and the onset of the sea breeze, which dramatically alters the vertical distribution of water vapor. If the underlying reanalysis  
452 climatology fails to adequately resolve the sharp moisture capping inversion at the top of the daytime planetary boundary layer  
453 (PBL), it will misrepresent the  $T_m$  weighting function. Specifically, if the model traps too much moisture near the intensely  
454 heated surface—or fails to capture the thermodynamic decoupling between the turbulent PBL and the stable free troposphere  
455 — the integral will disproportionately weight the hottest atmospheric layers. This coupled temperature-humidity mechanism  
456 physically manifests as the severe ~~diurnal bias peak 'noon ballooning'~~ effect observed in Fig. 7b, where the systematic bias  
457 surges to over +6 K. This demonstrates that high-precision GNSS meteorology requires synergistic MWR data to capture both  
458 the true thermal stability and the dynamic vertical moisture weighting of the atmosphere.

459



460  
461  
462  
463  
464

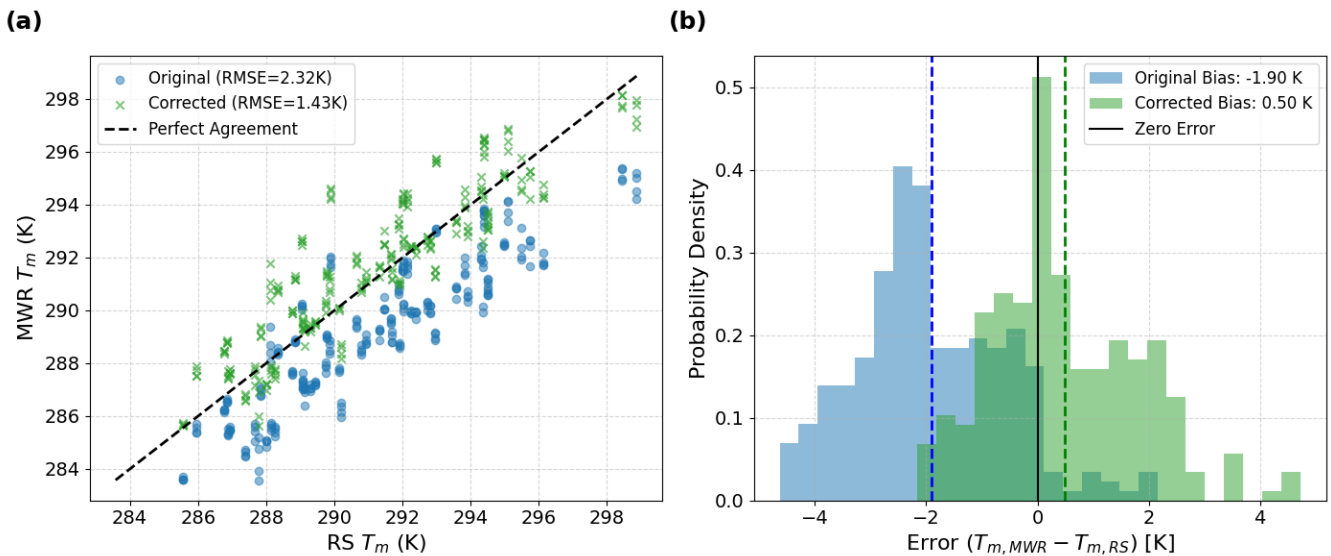
**Figure 7.** Diurnal variation of weighted mean atmospheric temperature  $T_m$  derived from microwave radiometer (MWR) observations and HGPT2 model simulations (top panel). The bottom panel shows the corresponding hourly mean bias ( $T_{m,HGPT2} - T_{m,MWR}$ ), with shaded envelopes indicating variability. The yellow shaded region highlights the period of maximum daytime heating.

### 465 3.4.2 Calibration and Bias Correction of MWR $T_m$

466 Fig. 8 presents a statistical validation of the MWR derived  $T_m$  against co-located RS observations. The analysis highlights the  
467 necessity and efficacy of a linear bias correction scheme to improve GNSS-PWV conversion accuracy. The scatter plot (Fig.  
468 2a) reveals a distinct systematic deviation in the original MWR retrieval relative to the RS reference. The data points  
469 consistently fall below the 1:1 identity line, indicating a negative bias in the raw MWR  $T_m$  product. The original RMSE is 2.32  
470 K. This error is largely driven by the systematic offset rather than random scatter, as evidenced by the high linearity ( $R^2$ ) of

471 the relationship. The thermodynamic profiles were retrieved using the manufacturer's standard Neural Network (NN)  
472 algorithm, trained on Region historical RS data.

473 The Probability Density Function (PDF) of the errors ( $T_{m,MWR}-T_{m,RS}$ ) in Fig. 8b clearly visualizes the bias shift. The pre-  
474 correction distribution is non-Gaussian and shifted significantly to the negative domain, with a mean bias ( $\mu$ ) of -1.90 K. In  
475 the context of GNSS meteorology, a  $T_m$  error of  $\approx 2$  K translates to a relative PWV error of approximately 0.7–1.0%. For  
476 climate monitoring, this represents a significant systematic dry bias. Applying the linear correction model ( $T_{m,corr}=\alpha T_{m,raw}+\beta$ )  
477 successfully re-centers the error distribution. The post-correction bias is reduced to 0.50 K, and the histogram aligns  
478 symmetrically around the zero-error line. The correction reduces the RMSE to 1.43 K, which is consistent with the theoretical  
479 accuracy limit of ground-based radiometric profiling (typically 1–2 K). The remaining spread (width of the green histogram)  
480 represents the random error component, likely attributable to instrumental noise and the imperfect spatiotemporal matching  
481 between the instantaneous MWR zenith view and the drifting radiosonde balloon. The correction methodology effectively  
482 removes the systematic instrumental bias without artificially compressing the natural variability of the atmosphere. The  
483 reduction of RMSE by  $\sim 38\%$  (from 2.32 K to 1.43 K) confirms that site-specific calibration of  $T_m$  is a mandatory processing  
484 step for generating climate-quality GNSS-PWV datasets.



485  
486 **Figure 8.** Evaluation of weighted mean temperature  $T_m$  correction against Radiosonde (RS) observations. (a) scatter plots of original and  
487 bias-corrected MWR-derived  $T_m$  versus RS  $T_m$ , with the dashed line indicating perfect agreement. (b) presents the probability density of  
488 errors ( $T_{m,MWR}-T_{m,RS}$ ) before and after correction, demonstrating a substantial reduction in cold bias and RMSE.  
489

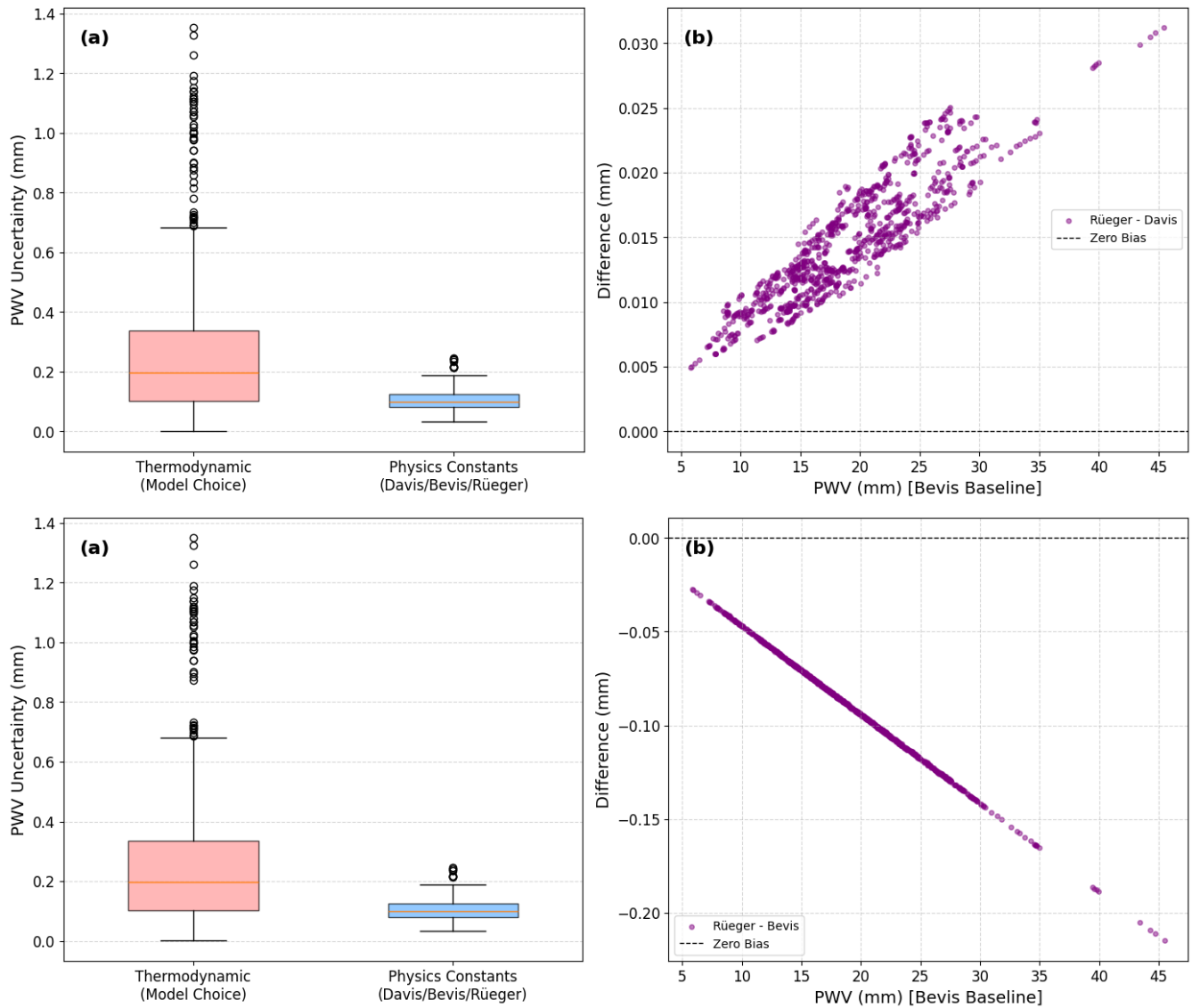


**Figure 9.** (a) PWV uncertainty attributed to thermodynamic assumptions and to the choice of refractivity constants. (b) Difference in GNSS-derived PWV resulting from the use of alternative refractivity constant formulations relative to Bevis et al. (1994).

In standard GNSS network processing, the largest source of PWV uncertainty is often the interpolation or modeling of surface pressure required to calculate the ZHD (Van Malderen et al., 2022). However, the CYGMEN observatory setup mitigates this spatial interpolation error by utilizing the co-located Vaisala WXT536 sensor, which has a stated pressure accuracy of  $\pm 0.5$  hPa. A 0.5 hPa pressure uncertainty propagates to approximately 1.15 mm of error in the ZHD. After applying the  $\Pi$  conversion factor, this restricts the pressure-induced PWV uncertainty to roughly  $\pm 0.17$  mm. Because this high-precision

501 localized pressure data effectively minimizes ZHD uncertainty, the accuracy of the  $T_m$  parameterization emerges as the  
502 dominant remaining variable in the PWV error budget for this site.

503 It is important to note that the complete error budget for GNSS-derived PWV encompasses significant uncertainties  
504 originating from the ZTD estimation phase itself. These include geodetic errors such as satellite orbit and clock uncertainties,  
505 mapping function inaccuracies, and site-dependent electromagnetic effects like signal scattering and multipath. While these  
506 geodetic factors are critical, the following component-wise uncertainty analysis (Fig. 9) specifically isolates the errors  
507 introduced during the subsequent conversion step ( $\Pi$ ). To decouple these retrieval contributions, two primary sources of  
508 uncertainty were isolated: the thermodynamic parameterization of  $T_m$  and the selection of atmospheric refractivity constants  
509 To decouple the error contributions in the GNSS PWV retrieval chain, a component-wise uncertainty analysis was performed  
510 focusing on the conversion factor,  $\Pi$ . Two primary sources of uncertainty were isolated: the thermodynamic parameterization  
511 of  $T_m$  and the selection of atmospheric refractivity constants ( $k_2', k_3$ ). —When decoupling these retrieval contributions, it is  
512 critical to distinguish between the statistical nature of the underlying error sources. As demonstrated by Healy (2011),  
513 uncertainties in the atmospheric refractivity constants ( $k_2', k_3$ ) act strictly as static systematic biases; selecting a different set of  
514 published constants permanently shifts the baseline of the  $\Pi$  by a fixed margin. Conversely, the uncertainty originating from  
515 the  $T_m$  parameterization is a dynamic, compound error. As highlighted by Wang et al. (2005) and Bock et al. (2021), empirical  
516  $T_m$  models derived from surface temperatures often fail to capture the true profile variance, introducing both a systematic bias  
517 (the model's mean regional offset) and a substantial random error component (the statistical scatter, or RMSE, driven by real-  
518 time thermodynamic variability and diurnal decoupling). While Fig. 9 juxtaposes these two distinct sources to illustrate their  
519 relative bounding magnitude on the final IWV product, their fundamentally different statistical behaviors—static bias versus  
520 dynamic scatter—must be acknowledged. As illustrated in Fig. 9(a), the uncertainty introduced by the  $T_m$  estimation strategy  
521 significantly outweighs the influence of the physical constants. Specifically, the stochastic variability from modeling  $T_m$   
522 (comparing HGPT2 climatology against direct radiometric observation) results in a retrieval error of approximately 1–2 mm.  
523 In contrast, the uncertainty associated with the choice of refractivity coefficients—defined here as the maximum divergence  
524 between the historical Davis et al. (1985), the standard Bevis et al. (1994), and the updated Rüeiger (2002) formulations—  
525 remains an order of magnitude smaller. Fig. 9(b) further resolves the impact of the refractivity constants, showing the  
526 differential bias between the oldest (Davis) and newest (Rüeiger) standards. The relationship is linear and proportional to the  
527 total water vapour content, consistent with a scaling of the  $\Pi$  factor. While the transition to the Rüeiger (2002) constants  
528 introduces a systematic positive shift, the magnitude of this correction (typically <0.2 mm for standard loading) is negligible  
529 for synoptic meteorological applications compared to the noise induced by  $T_m$  errors. However, for long-term climatological  
530 trend analysis where stability is paramount, consistent adherence to the Rüeiger (2002) standard is recommended to eliminate  
531 this small, but persistent systematic bias. Overall, the correction of the  $T_m$  is 2.5 times more important than selection of the  
532 constant.

534 **3.5 Error Propagation and Synergistic Retrieval Assessment**

535 In this section, the PWV was derived using bias-corrected mean temperature ( $T_m$ ) and constant values based on the study by  
536 Rüeiger (2002), as mentioned in the Sect. 3.4. The impact of  $T_m$  errors on the final PWV product was analyzed to quantify the  
537 benefits of the synergistic retrieval method. Fig. 10 visualizes the direct relationship between the relative error in  $T_m$  and the  
538 resulting relative error in PWV. The plot reveals a strictly linear relationship ( $R^2=0.984$ ) with a slope of 0.981. This confirms  
539 the theoretical approximation that  $(\Delta PWV/PWV) \approx (\Delta T_m/T_m)$ . The color gradient indicates that this linear error propagation  
540 holds true across all PWV magnitudes (from  $<10$  mm to  $>45$  mm). This implies that temperature errors propagate directly into  
541 moisture errors regardless of the humidity level, making accurate  $T_m$  crucial at all times. Fig. 11 investigates the systematic  
542 difference ( $\Delta PWV$ ) between the synergistic retrieval (using MWR  $T_m$ ) and a standard retrieval (using empirical  $T_m$ ) as a  
543 function of ~~moisture abundance~~ ~~thermodynamic severity~~ (PWV magnitude). For drier conditions (PWV  $< 25$  mm), the  
544 difference is minimal (near zero), and the uncertainty (shaded region) is low. This suggests that for low humidity, the choice  
545 of  $T_m$  source is less critical. As atmospheric moisture increases ( $> 25$  mm), a significant negative bias emerges. The curve dips  
546 sharply, reaching nearly  $-1.0$  mm at extreme humidity (45+ mm). The 'Systematic Bias Threshold'-'Critical Error Culmination'  
547 marker indicates that beyond 45 mm, the discrepancy exceeds 1.0 mm. The fact that the bias magnitude scales directly with  
548 total PWV provides physical confirmation that the error source is located in the boundary layer, where the bulk of the water  
549 vapour resides. The growing negative bias demonstrates that standard GNSS processing (using static models like HGPT2)  
550 systematically overestimates water vapour during extreme events compared to the more accurate synergistic method. Rather  
551 than extrapolating these localized errors to regional hydrological impacts, we emphasize the primary empirical observation:  
552 the systemic deviation of the standard empirical model scales proportionally with the magnitude of the PWV regime. Crucially,  
553 this systematic overestimation of moisture during extreme events is deeply intertwined with the diurnal cycle of the local  
554 atmosphere. This analysis quantifies the specific operational penalty of utilizing static climatological models in this region,  
555 demonstrating that HGPT2 incurs an IWV error exceeding  $1.0 \text{ kg m}^{-2}$  during severe thermodynamic events. As previously  
556 established (Fig. 7), the static HGPT2 model displays an exaggerated diurnal wave with an amplitude exceeding 8.5 K. Because  
557 the static model fails to account for the thermodynamic decoupling between the heated boundary layer and the cooler free  
558 troposphere during the day, this  $T_m$  error artificially inflates the amplitude of the GNSS-derived PWV diurnal cycle during  
559 peak solar insolation. By utilizing the synergistic retrieval approach, this spurious daytime moisture amplification is effectively  
560 mitigated. While further multi-site, long-term studies are required to assess the broader impacts on regional operational  
561 forecasting, our localized dataset clearly indicates that integrating real-time MWR thermal data successfully removes diurnal  
562 artifacts and reduces systematic measurement biases at this site.

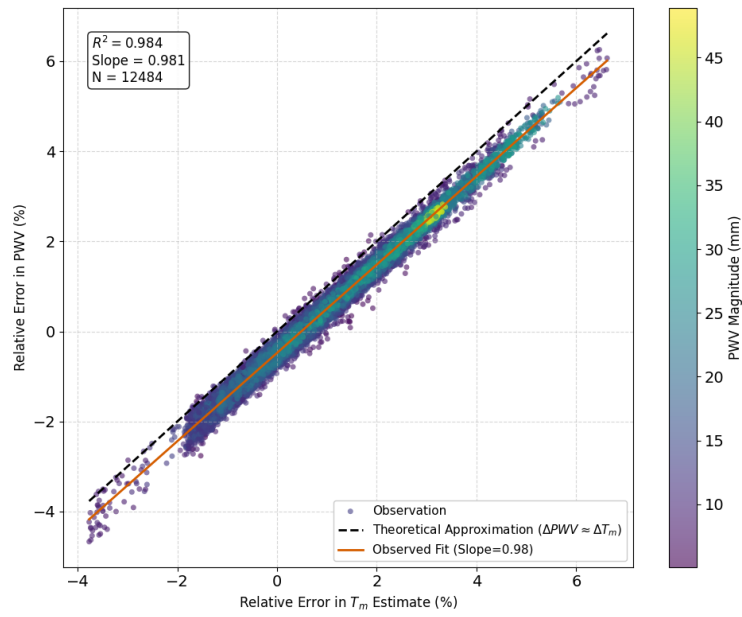
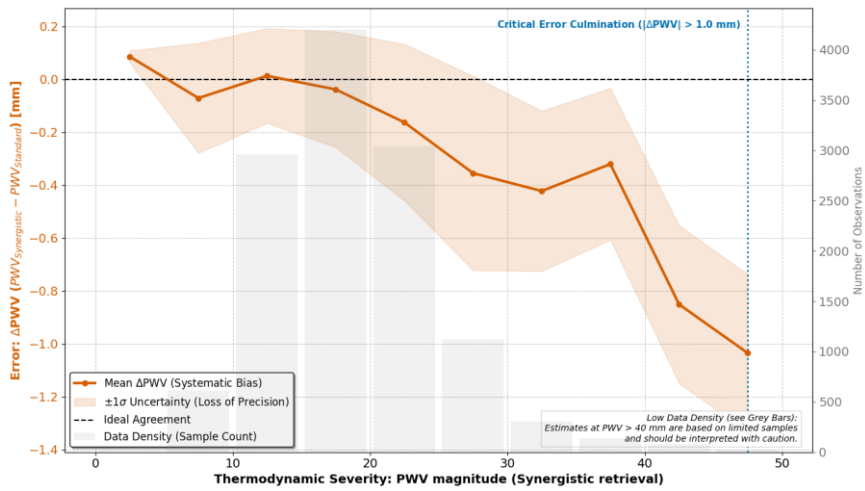
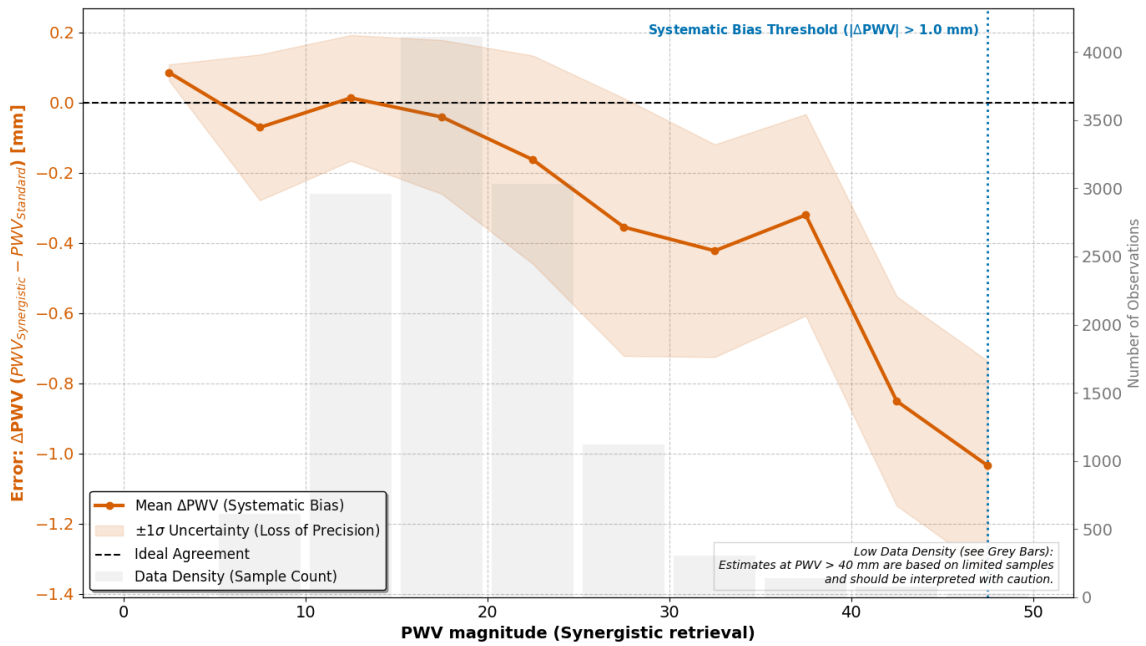


Figure 10. Driver of model failure: Impact of weighted mean temperature ( $T_m$ ) accuracy on PWV retrieval.



563  
564  
565

566



567  
568 **Figure 11.** Systematic breakdown and instability of the Standard GNSS model under extreme thermodynamic conditions.  
569

570 **4 Discussions**

571 The results of this study necessitate a fundamental re-evaluation of how  $T_m$  parameterization error, thermodynamic path delays  
572 are parameterized in GNSS meteorology, particularly within thermodynamically complex, semi-arid coastal environments like  
573 the Eastern Mediterranean (EM). The pronounced failure of the static HGPT2 model to capture the diurnal  $T_m$  cycle reveals a  
574 structural limitation inherent to empirical modeling. The observed "diurnal bias peak noon ballooning" effect is not merely a  
575 statistical anomaly; it represents a physical disconnect. Static empirical models rely heavily on  $T_s$ , effectively assuming that  
576 intense skin-level heating propagates uniformly through the atmospheric column. This assumption critically breaks down  
577 during the daytime in the EM, where the turbulent planetary boundary layer (PBL) aggressively decouples from the stable free  
578 troposphere. Evidence for this severe decoupling is explicitly documented in the high-vertical-resolution RS profiles collected  
579 during the campaign. Because the passive MWR struggles to effectively capture this sharp boundary—a direct result of the  
580 broad weighting functions and degraded vertical resolution inherent to its K-band observations—the instrument exhibits a  
581 'smoothing error' across the inversion layer. This structural limitation highlights exactly why applying a site-specific bias  
582 correction to the MWR's native output is a necessary prerequisite for precision GNSS meteorology. Furthermore, the failure  
583 of the reanalysis climatology to properly resolve the sharp moisture capping inversion during the onset of the daytime sea-  
584 breeze fundamentally corrupts the moisture-weighted  $T_m$  integral. Ground-based microwave radiometry overcomes this  
585 structural blindness by directly measuring the integrated thermal emissions of the column.

586 However, the performance of the MWR in this study highlights the duality of passive microwave remote sensing: it is highly  
587 proficient at retrieving integral quantities but degrades severely when resolving differential or gradient-based parameters. The  
588 successful reduction of the  $T_m$  RMSE via site-specific linear correction confirms that the MWR's K-band and V-band channels  
589 effectively capture the true thermal inertia of the troposphere. The initial systematic cold bias observed aloft is a known artifact  
590 of ill-posed neural network retrievals (Cimini et al., 2006; Löhnert and Maier, 2012). Because the vertical resolution of passive  
591 microwave observations degrades rapidly with height, the retrievals become heavily constrained by historical training datasets  
592 (the climatological prior), which often fail to capture localized, transition-season lapse rates in the free troposphere. The initial  
593 ~~systematic cold bias observed aloft is a known artifact of ill-posed neural network retrievals, which are heavily constrained by~~  
594 ~~historical training datasets that often fail to capture localized, transition-season lapse rates.~~ Conversely, the complete failure  
595 of the MWR to derive a physically realistic water vapour scale height ( $H_v$ ) exposes the "smoothing error" inherent to passive  
596 radiometry. Because the broad weighting functions of the K-band channels cannot resolve sharp boundary layer moisture  
597 inversions, the retrieval algorithm mathematically smears the moisture mass upward. This confirms that while MWR serves  
598 as a robust standard for total column mass, researchers must exercise extreme caution when utilizing its smoothed profiles to  
599 characterize vertical moisture compactness.

600 While this study relies on a single-site, multi-month dataset, the physical mechanisms identified have broad relevance beyond  
601 the Nicosia region. The Eastern Mediterranean serves as a highly representative climatic hotspot for semi-arid coastal  
602 environments experiencing enhanced warming and intensified hydrological cycles. It is important to note that the specific  
603 threshold of >45 mm identified here is characteristic of the climatological moisture capacity of the Eastern Mediterranean EM  
604 during extreme summer anomalies. While the exact numerical value of this 'Systematic Bias ThresholdCritical Error  
605 Culmination' will vary geographically depending on local atmospheric dynamics and latitude, the underlying physical principle  
606 remains universal: empirical  $T_m$  models systematically degrade proportionally to the total atmospheric moisture mass during  
607 severe local extremes. The core vulnerability exposed in this research—that static global models are structurally blind to sharp  
608 boundary layer thermodynamic decoupling during peak insolation—is a fundamental physics problem, not a local anomaly.  
609 Therefore, the proposed synergistic MWR-GNSS retrieval architecture provides a universally applicable solution for  
610 mitigating systematic dry biases in any complex terrain or coastal environment globally. While the simple linear regression  
611 applied in this study proved highly effective at correcting systematic  $T_m$  biases for operational GNSS conversions, there  
612 remains room for algorithmic improvement. As the CYGMEN infrastructure accumulates a multi-year climatological database  
613 of high-resolution radiosonde profiles, future work should focus on complementary Neural Network (NN) training. By  
614 retraining the MWR retrieval algorithms using site-specific radiative transfer modeling rather than relying on the  
615 manufacturer's regional historical priors, the native temperature and humidity profiles can be further optimized at the retrieval  
616 level.

617 Finally, our component-wise uncertainty analysis clarifies the error propagation chain in the GNSS-PWV conversion process,  
618 shifting the paradigm of where optimization efforts should be focused. Historically, significant effort within the geodetic  
619 community has been expended on refining atmospheric refractivity constants. However, we demonstrate that the error induced  
620 by transitioning from the historical Davis et al. (1985) formulations to the modern Rüeiger (2002) constants is practically  
621 negligible ( $<0.2$  mm) for synoptic meteorological applications. The true "weak link" in the retrieval chain is unequivocally the  
622 thermodynamic parameterization, which introduces errors an order of magnitude larger.

623

## 624 **5 Conclusion**

625 This study demonstrated that the accuracy of GNSS-derived Precipitable Water Vapour (PWV) in the Eastern Mediterranean  
626 region, is ~~fundamentally limited~~significantly affected by the thermodynamic rigidity of static climatological models. By  
627 implementing a synergistic retrieval strategy that couples GNSS delays with real-time ground-based microwave radiometry  
628 (MWR), we successfully quantified and mitigated these limitations. The investigation yielded three primary methodological  
629 conclusions. First, we established that standard empirical models (e.g., HGPT2) are structurally incapable of resolving the  
630 diurnal thermodynamic decoupling between the boundary layer and free troposphere. This deficiency leads to severe  
631 systematic errors (the "~~diurnal bias peaknoon ballooning~~" effect) exceeding 6 K in weighted mean temperature ( $T_m$ ) during  
632 peak solar insolation, which directly propagates into a PWV bias  $>1.0$  mm during extreme hygrometric events. Second, the  
633 MWR proved to be a superior source for  ~~$T_m$  parameterization errors~~thermodynamic path delays, provided that site-specific  
634 calibration is applied. The development of a linear bias correction scheme reduced the MWR  $T_m$  root-mean-square error from  
635 2.32 K to 1.43 K. This correction substantially reduces the conversion-related uncertainty in the GNSS water vapour product  
636 compared to standard climatological approaches. Third, the component-wise sensitivity analysis confirmed that  
637 thermodynamic parameterization is a highly significant source of uncertainty that exacerbates existing geodetic ZTD errors,  
638 outweighing uncertainties in refractive index constants by an order of magnitude. Consequently, the proposed combined  
639 retrieval represents a highly valuable architectural upgrade for monitoring severe weather in complex coastal environments  
640 like the Eastern Mediterranean. However, it must be acknowledged that there are many sites worldwide where the deployment  
641 of microwave radiometers may not be justified. Given the high capital and operational costs of radiometric hardware, the  
642 presence of other unmitigated geodetic uncertainties, and the adequate performance of static  $T_m$  models in less  
643 thermodynamically complex regions, this synergistic approach is best reserved for targeted deployments in highly vulnerable  
644 climatic hotspots.

645 ~~The development of a linear bias correction scheme reduced the MWR  $T_m$  root mean square error from 2.32 K to 1.43 K. This~~  
646 ~~correction effectively halves the uncertainty in the final GNSS water vapor product compared to standard climatological~~  
647 ~~approaches. Third, the sensitivity analysis confirmed that thermodynamic input quality is the dominant error source in GNSS~~

648 ~~meteorology, outweighing uncertainties in refractive index constants by an order of magnitude. Consequently, the proposed~~  
649 ~~combined retrieval is not merely an incremental improvement but a necessary architectural upgrade for monitoring severe~~  
650 ~~weather.~~ For the climate-sensitive Eastern Mediterranean EM-region, relying on static models for GNSS processing risks  
651 systematically masking moisture trends during heatwaves and deep convection. We therefore recommend the operational  
652 integration of collocated MWR observations into national GNSS processing chains. Where collocation is not feasible, future  
653 work should focus on assimilating MWR-derived diurnal shape functions into static models to bridge the gap between  
654 climatology and reality. This study establishes the "Corrected Synergistic Method" as a robust benchmark for generation of  
655 climate-quality water vapour datasets in complex thermodynamic environments.

### 657 **Data availability**

658 The MWR and GNSS data used in this study are available from the CYGMEN project archive upon request. High resolution  
659 Radiosonde data available from the Department of Meteorology (DoM), Cyprus. The ERA5 reanalysis data can be downloaded  
660 from the Copernicus Climate Change Service (C3S) Climate Data Store.

### 662 **Author contributions**

663 ANP carried out the GNSS, MWR, and Radiosonde data processing, performed the synergistic PWV retrievals and error  
664 diagnosis, and wrote the initial version of the paper. CO and HH conceptualized the study, acquired the funding and resources  
665 for the CYGMEN infrastructure, and supervised the investigation. All authors discussed the results, edited, and proofread the  
666 paper..

### 668 **Competing interests**

669 All authors declare that they have no conflict of interest.

### 671 **Acknowledgements**

672 We would like to express our sincere gratitude to the Cyprus Department of Meteorology (DoM) and in particular to Physicist  
673 and Meteorology Officer Dr. Demetris Charalambous, for his invaluable guidance and for providing access to essential  
674 resources at Athalassa observatory in Nicosia, Cyprus.

676 **Financial support**

677 The present study is funded by the Strategic Infrastructure project CYGMEN, which is implemented in the frames of Cohesion  
678 Policy Programme “THALIA 2021-2027” and is co-funded by the European Union.

679

680 **References**

681 Askne, J. and Nordius, H.: Estimation of tropospheric delay for microwaves from surface weather data, *Radio Sci.*, 22, 379–  
682 386, <https://doi.org/10.1029/RS0221003p00379>, 1987.

683 Bennartz, R. and Bauer, P.: Sensitivity of microwave radiances at 85–183 GHz to precipitating ice particles, *Radio Sci.*, 38,  
684 8075, <https://doi.org/10.1029/2002RS002626>, 2003.

685 Bennett, G. V. and Jupp, A.: Operational assimilation of GPS zenith total delay observations into the Met Office numerical  
686 weather prediction models, *Mon. Weather Rev.*, 140, 2706–2719, <https://doi.org/10.1175/MWR-D-11-00156.1>, 2012.

687 Bevis, M., Businger, S., Herring, T. A., Rocken, C., Anthes, R. A., and Ware, R. H.: GPS meteorology: Remote sensing of  
688 atmospheric water vapor using the Global Positioning System, *J. Geophys. Res.*, 97, 15787–15801,  
689 <https://doi.org/10.1029/92JD01517>, 1992.

690 Bevis, M., Businger, S., Chiswell, S., Herring, T. A., Anthes, R. A., Rocken, C., and Ware, R. H.: GPS meteorology: Mapping  
691 zenith wet delays onto precipitable water, *J. Appl. Meteorol.*, 33, 379–386, [https://doi.org/10.1175/1520-0450\(1994\)033<0379:GMMZWD>2.0.CO;2](https://doi.org/10.1175/1520-0450(1994)033<0379:GMMZWD>2.0.CO;2), 1994.

693 Böhm, J., Möller, G., Schindelegger, M., Pain, G., and Weber, R.: Development of an improved empirical model for slant  
694 delays in the troposphere (GPT2w), *GPS Solut.*, 19, 433–441, <https://doi.org/10.1007/s10291-014-0403-7>, 2015.

695 Bolton, D.: The computation of equivalent potential temperature, *Mon. Weather Rev.*, 108, 1046–1053,  
696 [https://doi.org/10.1175/1520-0493\(1980\)108<1046:TCOEPT>2.0.CO;2](https://doi.org/10.1175/1520-0493(1980)108<1046:TCOEPT>2.0.CO;2) 1980.

697 Brenot, H., Neméghaire, J., Delobbe, L., Clerbaux, N., De Meutter, P., Deckmyn, A., Delcloo, A., Frappez, L., and Van  
698 Roozendael, M.: Preliminary signs of the initiation of deep convection by GNSS, *Atmos. Chem. Phys.*, 13, 5425–5449,  
699 <https://doi.org/10.5194/acp-13-5425-2013>, 2013.

700 [Bock, O., Bossler, P., Flamant, C., Doerflinger, E., Jansen, F., Fages, R., Bony, S. and Schnitt, S.: Integrated water vapour](#)  
701 [observations in the Caribbean arc from a network of ground-based GNSS receivers during EUREC 4 A. \*Earth System Science\*](#)  
702 [\*Data\*, 13\(5\), pp.2407-2436. <https://doi.org/10.5194/essd-13-2407-2021>. 2021.](#)

703 Cimini, D., Westwater, E. R., Gasiewski, A. J., Klein, M., Leuski, V. Y., and Dowlatshahi, S.: Thermodynamic atmospheric  
704 profiling during the 2010 Winter Olympics using ground-based microwave radiometry, *IEEE T. Geosci. Remote*, 49, 4959–  
705 4969, <https://doi.org/10.1109/TGRS.2011.2154337>, 2011.

706 [Cimini, Domenico, Tim J. Hewison, Lorenz Martin, Jürgen Güldner, Catherine Gaffard, and Frank S. Marzano. "Temperature](#)  
707 [and humidity profile retrievals from ground-based microwave radiometers during TUC." \*Meteorologische Zeitschrift\* 15, no.](#)  
708 [1: 45-56. 2006.](#)

709 Crewell, S. and Löhnert, U.: Accuracy of boundary layer temperature profiles retrieved with multifrequency multiangle  
710 microwave radiometry, *IEEE T. Geosci. Remote*, 45, 2195–2201, [doi: 10.1109/TGRS.2006.888434](https://doi.org/10.1109/TGRS.2006.888434). 2007.

711 Douša, J. and Václavovic, P.: Real-time zenith tropospheric delays in support of numerical weather prediction applications,  
712 *Adv. Space Res.*, 53, 1347–1358, <https://doi.org/10.1016/j.asr.2014.02.021>, 2014.

713 Davis, J. L., Herring, T. A., Shapiro, I. I., Rogers, A. E. E., and Elgered, G.: Geodesy by radio interferometry: Effects of  
714 atmospheric modeling errors on estimates of baseline length, *Radio Sci.*, 20, 1593–1607,  
715 <https://doi.org/10.1029/RS020i006p01593>, 1985.

716 Gaffen, D. J.: Temporal inhomogeneities in radiosonde temperature records, *J. Geophys. Res.*, 99, 3667–3676,  
717 <https://doi.org/10.1029/93JD03179>, 1994.

718 Giannadaki, D., Oikonomou, C., Haralambous, H., Tymvios, F., and Loizou, E.: Validation of precipitable water vapour  
719 products using CyMETEO GNSS network in Cyprus, in: Eleventh International Conference on Remote Sensing and  
720 Geoinformation of the Environment (RSCy2025), Vol. 13816, 397–409, SPIE, 2025.

721 Giorgi, F.: Climate change hot-spots, *Geophys. Res. Lett.*, 33, L08707, <https://doi.org/10.1029/2006GL025734>, 2006

722 Guerova, G., Jones, J., Douša, J., Dick, G., de Haan, S., Pottiaux, E., Bock, O., Pacione, R., Elgered, G., Vedel, H., and Bender,  
723 M.: Review of the state of the art and future prospects of the ground-based GNSS meteorology in Europe, *Atmos. Meas. Tech.*,  
724 9, 5385–5406, <https://doi.org/10.5194/amt-9-5385-2016>, 2016.

725 Held, I. M. and Soden, B. J.: Robust responses of the hydrological cycle to global warming, *J. Climate*, 19, 5686–5699,  
726 <https://doi.org/10.1175/JCLI3990.1>, 2006.

727 [Healy, S.B.: Refractivity coefficients used in the assimilation of GPS radio occultation measurements. \*Journal of Geophysical\*](#)  
728 [Research: Atmospheres](#), 116(D1). <https://doi.org/10.1029/2010JD014013>. 2011.

729 Jiang, P., Ye, S., Chen, D., Liu, Y., and Xia, P.: Development of time-varying global gridded Ts-Tm model for precise GPS-  
730 PWV retrieval, *Atmos. Meas. Tech.*, 12, 1233–1249, <https://doi.org/10.5194/amt-12-1233-2019>, 2019.

731 Jones, J., Guerova, G., Douša, J., Dick, G., de Haan, S., Pottiaux, E., Bock, O., Pacione, R., Elgered, G., Vedel, H., and Bender,  
732 M.: Advanced GNSS Tropospheric Products for Monitoring Severe Weather Events and Climate, Springer, Cham,  
733 <https://doi.org/10.1007/978-3-030-13901-8>~~<https://doi.org/10.1007/978-3-030-28909-6>~~, 2020.

734 Kiehl, J. T. and Trenberth, K. E.: Earth's annual global mean energy budget, *B. Am. Meteorol. Soc.*, 78, 197–208,  
735 [https://doi.org/10.1175/1520-0477\(1997\)078<0197:EAGMEB>2.0.CO;2](https://doi.org/10.1175/1520-0477(1997)078<0197:EAGMEB>2.0.CO;2), 1997.

736 Lan, Z., Zhang, B., and Geng, T.: Establishment and analysis of global gridded Tm-Ts relationship model, *Geodesy and*  
737 *Geodynamics*, 7, 101–107, <https://doi.org/10.1016/j.geog.2016.02.001>, 2016.

738 Lelieveld, J., Hadjinicolaou, P., Kostopoulou, E., Chenoweth, J., El Maayar, M., Giannakopoulos, C., Hannides, C., Lange,  
739 M. A., Tanarhte, M., Tyrlis, E., and Xoplaki, E.: Climate change and impacts in the Eastern Mediterranean and the Middle  
740 East, *Climatic Change*, 114, 667–687, <https://doi.org/10.1007/s10584-012-0418-4>, 2012.

741 Li, H., Wang, X., Wu, S., Zhang, K., Chen, X., Qiu, C., Zhang, Q., and Li, L.: Development of an improved model for  
742 prediction of short-term heavy precipitation based on GNSS-derived PWV, *Remote Sens.*, 12, 4101,  
743 <https://doi.org/10.3390/rs12244101>, 2020.

744 Löhnert, U. and Maier, O.: Operational profiling of temperature using ground-based microwave radiometry at Payerne:  
745 Prospects and challenges, *Atmos. Meas. Tech.*, 5, 1121–1134, <https://doi.org/10.5194/amt-5-1121-2012>, 2012.

746 Mateus, P., Mendes, V. B., and Plecha, S. M.: HGPT2: an ERA5-based global model to estimate relative humidity, *Remote*  
747 *Sens.*, 13, 2179, <https://doi.org/10.3390/rs13112179>, 2021.

748 Ning, T. and Elgered, G.: Intercomparison of MAX-DOAS vertical profile retrieval algorithms: studies on field data from the  
749 CINDI-2 campaign, *Atmos. Meas. Tech.*, 14, 1–35, <https://doi.org/10.5194/amt-14-1-2021>, 2021.

750 [Ning, Tong, J. Wang, G. Elgered, G. Dick, J. Wickert, Markus Bradke, M. Sommer, R. Querel, and D. Smale. "The uncertainty](https://doi.org/10.5194/amt-9-79-2016)  
751 [of the atmospheric integrated water vapour estimated from GNSS observations." \*Atmospheric Measurement Techniques\* 9, no.](https://doi.org/10.5194/amt-9-79-2016)  
752 [1. 79-92. doi:10.5194/amt-9-79-2016. 2016.](https://doi.org/10.5194/amt-9-79-2016)

753 Pakkattil, A., Parde, A. N., Wagh, S., Lonkar, P., and Ghude, S. D.: Wintertime Intercomparison of Specific Humidity and  
754 Temperature Profiles Measured by Microwave Radiometer (MWR), Radiosonde, and INSAT-3DR Sounder Over Delhi, India,  
755 *J. Geophys. Res. Atmos.*, 130, e2025JD044462, <https://doi.org/10.1029/2025JD044462>, 2025.

756 Parde, A. N., Ghude, S. D., Prasad, V. S., Hari Prasad, K. B. R. R., Dhangar, N. G., Lonkar, P., and Rajeevan, M.: Influence  
757 of ground-based microwave radiometer profile assimilation on fog genesis forecasts in the winter boundary layer of Northern  
758 India, *J. Geophys. Res. Atmos.*, 130, e2024JD042224, <https://doi.org/10.1029/2024JD042224>, 2025.

759 Oikonomou, C., Tymvios, F., Pikridas, C., Bitharis, S., Balidakis, K., Michaelides, S., ... and Charalambous, D.: Tropospheric  
760 delay performance for GNSS integrated water vapor estimation by using GPT2w model, ECMWF's IFS operational model and  
761 in situ meteorological data, *Adv. Geosci.*, 45, 363–375, <https://doi.org/10.5194/adgeo-45-363-2018>, 2018.

762 Realini, E., Gatti, A., Reguzzoni, M., Sampietro, D., and Venuti, G.: GNSS-based precipitable water vapor retrieval for severe  
763 weather monitoring: The 2014 Genoa flood case study, *Adv. Space Res.*, 53, 1–10, <https://doi.org/10.1016/j.asr.2014.02.015>,  
764 2014.

765 Rüeger, J. M.: Refractive index formulae for radio waves, in: Proceedings of the FIG XXII International Congress,  
766 Washington, D.C., USA, 19–26 April 2002, 1–13, 2002.

767 Ross, R. J. and Elliott, W. P.: Tropospheric water vapor climatology and trends over North America: 1973–93, *J. Climate*, 9,  
768 3561–3574, [https://doi.org/10.1175/1520-0442\(1996\)009<3561:TWVCAT>2.0.CO;2](https://doi.org/10.1175/1520-0442(1996)009<3561:TWVCAT>2.0.CO;2). 1996.

769 Saastamoinen, J.: Atmospheric correction for the troposphere and stratosphere in radio ranging satellites, in: The Use of  
770 Artificial Satellites for Geodesy, *Geophys. Monogr. Ser.*, 15, 247–251, AGU, Washington, D.C.,  
771 <https://doi.org/10.1029/GM015p0247>, 1972.

772 Soden, B. J. and Lanzante, J. R.: An assessment of satellite and radiosonde climatologies of upper-tropospheric water vapor,  
773 *J. Climate*, 9, 1235–1250, [https://doi.org/10.1175/1520-0442\(1996\)009<1235:AAOSAR>2.0.CO;2](https://doi.org/10.1175/1520-0442(1996)009<1235:AAOSAR>2.0.CO;2), 1996.

774 Steinke, S., Ebell, K., Löhnert, U., Bozzo, A., Crewell, S., and Turner, D. D.: Assessment of small-scale integrated water  
775 vapour variability during HOPE, *Atmos. Chem. Phys.*, 15, 2675–2692, <https://doi.org/10.5194/acp-15-2675-2015>, 2015.

776 Thayer, G. D.: An improved equation for the radio refractive index of air, *Radio Sci.*, 9, 803–807,  
777 <https://doi.org/10.1029/RS009i010p00803>, 1974.

778 Trenberth, K. E., Fasullo, J., and Smith, L.: Trends and variability in column-integrated atmospheric water vapor, *Clim.*  
779 *Dynam.*, 24, 741–758, <https://doi.org/10.1007/s00382-005-0017-4>, 2005.

780 Tomasi, C.: Vertical distribution features of atmospheric water vapor in the Mediterranean, Red Sea, and Indian Ocean, *J.*  
781 *Geophys. Res.*, 89, 2563–2566, <https://doi.org/10.1029/JD089iD02p02563>, 1984.

- 782 Van Malderen, R., Brenot, H., Pottiaux, E., Beirle, S., Hermans, C., De Mazière, M., ... and Bruyninx, C.: A multi-site  
783 intercomparison of integrated water vapour observations for climate change analysis, *Atmos. Meas. Tech.*, 7, 2487–2512,  
784 <https://doi.org/10.5194/amt-7-2487-2014>, 2014.
- 785 Van Malderen, R., Pottiaux, E., Klos, A., Domonkos, P., Elias, M., Ning, T., ... and Bock, O.: Homogenizing GPS precipitable  
786 water vapor time series: Benchmarking homogenization algorithms on synthetic datasets, *Remote Sens.*, 14, 1050,  
787 <https://doi.org/10.3390/rs14041050>, 2022.
- 788 Vaquero-Martínez, J., Antón, M., Ortiz de Galisteo, J. P., Cachorro, V. E., Wang, H., González-Abad, G., ... and Costa, M. J.:  
789 Inter-comparison of integrated water vapor from ground-based GPS and satellite remote sensing at Mediterranean sites, *IEEE*  
790 *J. Sel. Top. Appl.*, 11, 1718–1728, <https://doi.org/10.1109/JSTARS.2018.2812804>, 2018.
- 791 Weaver, C. P. and Ramanathan, V.: Deductions from a simple climate model: Factors governing surface temperature and  
792 atmospheric thermal structure, *J. Geophys. Res.*, 100, 11585–11591, <https://doi.org/10.1029/95JD00774>, 1995.
- 793 [Wang, Junhong, Liangying Zhang, and Aiguo Dai. "Global estimates of water-vapor-weighted mean temperature of the](#)  
794 [atmosphere for GPS applications." \*Journal of Geophysical Research: Atmospheres\* 110, no. D21. doi:10.1029/2005JD006215.](#)  
795 [2005.](#)
- 796 Yao, Y., Zhang, B., Yue, S., Xu, C., and Peng, W.: Analysis of the global Tm-Ts correlation and establishment of the latitude-  
797 related linear model, *Chin. Sci. Bull.*, 59, 2340–2347, <https://doi.org/10.1007/s11434-014-0275-9>, 2014.
- 798 Ziskin Ziv, S., Yair, Y., Alpert, P., Uzan, L., and Reuveni, Y.: The diurnal variability of precipitable water vapor derived from  
799 GPS tropospheric path delays over the Eastern Mediterranean, *Atmos. Res.*, 249, 105307,  
800 <https://doi.org/10.1016/j.atmosres.2020.105307>, 2021.
- 801 Ziskin Ziv, S., Alpert, P., and Reuveni, Y.: Long-term variability and trends of precipitable water vapour derived from GPS  
802 tropospheric path delays over the Eastern Mediterranean, *Int. J. Climatol.*, 41, 6433–6454, <https://doi.org/10.1002/joc.7205>,  
803 2021.
- 804 Zittis, G., Hadjinicolaou, P., Klangidou, M., et al.: A multi-model, multi-scenario, and multi-domain analysis of regional  
805 climate projections for the Mediterranean, *Reg. Environ. Change*, 19, 2621–2635, [https://doi.org/10.1007/s10113-019-01565-](https://doi.org/10.1007/s10113-019-01565-w)  
806 [w](https://doi.org/10.1007/s10113-019-01565-w), 2019.